Title

Increasing reactivity by incorporating π-acceptor ligands into coordinatively unsaturated thiolate-ligated iron(II) complexes

Authors

Toledo, Santiago
Yan Poon, Penny Chaau
Gleaves, Morgan
et al.

Publication Date

2021-09-01

DOI

10.1016/j.ica.2021.120422

Peer reviewed

Published in final edited form as:

Inorganica Chim Acta. 2021 September 1; 524: . doi:10.1016/j.ica.2021.120422.

Increasing reactivity by incorporating π-acceptor ligands into coordinatively unsaturated thiolate-ligated iron(II) complexes

Santiago Toledo, **Penny Chaau Yan Poon**, **Morgan Gleaves**, **Julian Rees**, **Dylan M. Rogers**[1], **Werner Kaminsky**[1], **Julie A. Kovacs**[*]

The Department of Chemistry, University of Washington, Box 351700 Seattle, WA 98195-1700, United States

Abstract

Reported herein is the structural, spectroscopic, redox, and reactivity properties of a series of iron complexes containing both a π-donating thiolate, and π-accepting *N*-heterocycles in the coordination sphere, in which we systematically vary the substituents on the *N*-heterocycle, the size of the *N*-heterocycle, and the linker between the imine nitrogen and tertiary amine nitrogen. In contrast to our primary amine/thiolate-ligated Fe(II) complex, $[Fe^{II}(S^{Me2}N_4(tren))]^+$ (**1**), the Fe(II) complexes reported herein are intensely colored, allowing us to visually monitor reactivity. Ferrous complexes with R = H substituents in the 6-position of the pyridines, $[Fe^{II}(S^{Me2}N_4(6\text{-H-DPPN})]^+$ (**6**) and $[Fe^{II}(S^{Me2}N_4(6\text{-H-DPEN}))(MeOH)]^+$ (**8-MeOH**) are shown to readily bind neutral ligands, and all of the Fe(II) complexes are shown to bind anionic ligands regardless of steric congestion. This reactivity is in contrast to **1** and is attributed to an increased metal ion Lewis acidity assessed via aniodic redox potentials, $E_{p,a}$, caused by the π-acid ligands. Thermodynamic parameters (ΔH, ΔS) for neutral ligand binding were obtained from *T*-dependent equilibrium constants. All but the most sterically congested complex, $[Fe^{II}(S^{Me2}N_4(6\text{-Me-DPPN})]^+$ (**5**), react with O_2. In contrast to our Mn(II)-analogues, dioxygen intermediates are not observed. Rates of formation of the final mono oxo-bridged products were assessed via kinetics and shown to be inversely dependent on redox potentials, $E_{p,a}$, consistent with a mechanism involving electron transfer.

Keywords

Iron thiolate structures; Thermodynamics of ligand binding; Dioxygen reactivity

[*]Corresponding author. kovacs@chem.washington.edu (J.A. Kovacs).

[1]UW Staff Crystallographer.

CRediT authorship contribution statement

Santiago Toledo: Data curation, Writing - original draft. **Penny Chaau Yan Poon:** Data curation. **Morgan Gleaves:** Data curation. **Julian Rees:** Data curation. **Dylan M. Rogers:** Formal analysis. **Werner Kaminsky:** Formal analysis. **Julie A. Kovacs:** Conceptualization, Funding acquisition, Supervision, Writing - review & editing.

Declaration of Competing Interest

The authors declare that they have no known competing financial interests or personal relationships that could have appeared to influence the work reported in this paper.

Appendix A. Supplementary data

Supplementary data to this article can be found online at https://doi.org/10.1016/j.ica.2021.120422.

1. Introduction

Thiolate ligands have been shown to lower the activation barrier to dioxygen binding, increase the ability of Fe–$O_2^{\bullet -}$ superoxo compounds to abstract H-atoms from strong C–H bonds [1], promote peroxo O–O bond cleavage [2], and create potent high-valent metal-oxos capable of activating strong C–H bonds [1,3–5]. Iron thiolate (Fe–SR) bonds are highly covalent, stabilize low spin-states due to the nephelauxetic effect [6], and are capable of compensating for changes in electron density at the metal ion thereby maintaining a relatively constant redox potential [7]. This compensatory effect reflects not only the highly covalent Fe-S bonds, but also the redox non-innocence of thiolate ligands, which facilitates delocalization of oxidizing equivalents onto the sulfur [8]. This unique property is important to the function of both electron-transfer proteins, such as blue copper proteins [9,10], as well as non-heme iron enzymes [11], such as isopenicillin *N*-synthase (IPNS) [3,12,13], superoxide reductase (SOR) [14–19], cysteine dioxygenases (CDO) [20–26], and nitrile hydratases (NHases) [27–31], as well as the heme enzyme cytochrome P450 [32–34].

The primary coordination sphere of a transition-metal complex can have a profound influence on the electronic and geometric structure, as well as its magnetic, redox, and reactivity properties. Even subtle changes to the coordination sphere, involving the replacement of a single hydrogen-bond [35–38], or protonation of a coordinated ligand [7,39], can dramatically alter these properties. For example, if the imidazole of haemoglobin [38,39] is replaced with a cysteinate [5,40], then O_2 activation and reduction, and peroxo O–O bond cleavage, as opposed to O_2 transport, is favored, and the resulting iron-oxo becomes a potent oxidant capable of cleaving strong C–H bonds [5,40]. Our work has shown that thiolate ligands make low–spin iron accessible even in a non–heme environment [30,41,42], stabilize iron in the +3 oxidation state [30,41,42], and labilize sites *trans* to the thiolate thereby promoting reactivity by releasing product [15], even with low–spin Co(III) which is typically inert [43,44].

Previously our group showed that thiolate-ligated $[Fe^{II}(S^{Me2}N_4(tren))]^+$ (**1**, Scheme 1) reacts with superoxide in a proton-dependent mechanism to afford a well-characterized metastable hydroperoxo complex, $[Fe^{III}(S^{Me2}N_4(tren))(OOH)]^+$ (**2**), which then releases H_2O_2 upon protonation at the proximal oxygen [45], thus mimicking the function of SOR [46,47]. Two potential mechanisms for both the formation of **2**, as well as the SOR ferric hydroperoxo intermediate, would involve the sequential addition of $O_2^{\bullet -}$ and a proton, (a) + (b) to afford an Fe(II) — $O_2^{-\bullet}$, followed by Fe(III)–$_{OOH}$ intermediate (Fig. 1), or the concerted addition of HO_2 to the metal ion (pathway (c) of Fig. 1). Primary amine-ligated **1**, the precursor to hydroperoxo **2**, is colorless and only displays bands in the UV, due to the high energy of the S → Fe(II) CT band [45,48]. This makes it difficult to detect ferrous Fe (II)-L (e.g., L = O_2^-) intermediates. By incorporating **π**-acceptor *N*-heterocycles (N^{Ar}) into the ligand scaffold (Figs. 2 and 3), it should be easier to monitor reactivity via electronic absorption spectroscopy using the M → **π**-acceptor chromophore. We recently showed that steric encumbering groups (Me, OMe, or benzo) on the N^{Ar} ligand influence the kinetic barrier to O_2 binding to Mn(II), peroxo O–O bond cleavage, and hydrogen atom transfer (HAT) reactivity of the corresponding high-valent Mn-oxo intermediates [49,50]. We have also

shown that the combination of redox active π-accepting *N*-heterocycle ligands and π-donor thiolate ligands can have a profound effect on the electronic structure. Sulfur K-edge X-ray absorption spectroscopic (XAS) data coupled with time-dependent density functional theory calculations (TD DFT) provided evidence for direct communication between the thiolate sulfur of $\left[Fe^{II}(tame-N_2S(py)_2)\right]_2^{2+}$ and the roughly orthogonal (α-imino)-*N*-heterocycle ligand π*-orbitals [8]. Extensive delocalization of bonding electrons over the sulfur, iron, and (α-imino)-*N*-heterocycle was observed in the frontier orbitals, and the α-imino-pyridine C=N and C^{ipso}-C bonds were shown to elongate close to the length of a reduced α-imino-pyridine moiety, even in the absence of a strong reducing agent [8].

Herein we report the synthesis, structure, redox properties, and reactivity of a new series of structurally related 5-coordinate thiolate-ligated Fe(II) complexes (Scheme 1) that incorporate both a π-donating thiolate ligand and π- accepting pyridine or quinoline ligands (Figs. 2 and 3). We show that by incorporating π-accepting *N*-heterocycles (N^{Ar} = 6-H-pyridine, 6-Me-pyridine, or quinoline) in place of the primary amines of $[Fe^{II}(S^{Me2}N_4(tren))]^+$ (**1**) that (a) the ferrous compounds are intensely colored making it is easier to monitor reactions via electronic absorption spectroscopy, (b) the binding affinity for a sixth ligand increases, and (c) metal ion Lewis acidity increases [51].

2. Results and discussion

2.1. Syntheses and structure of coordinatively unsaturated Fe(II) complexes containing both a π-accepting N-heterocycle and a π-donating thiolate

The *N*-heterocycle ligands used in this study (Fig. 4) were synthesized as previously described for the corresponding Mn-derivatives [52]. The ligand scaffold was varied to include (a) pyridine or quinoline *N*-heterocycles, (b) H or Me substituents on the pyridine rings, or (c) ethyl versus propyl linkers between the tertiary amine and imine nitrogens (Fig. 4, highlighted in red) [52]. A metal templated Schiff-base reaction was used to assemble the corresponding Fe(II) complexes (Scheme 1, Figs. 2, 3, 5, and 10). Single crystals of each complex were obtained as described in the supplemental material. Crystallographic tables are provided in the supplemental material (Tables S5–S39). Selected metrical parameters are assembled in Table 1. As shown in the ORTEP diagrams of Figs. 2,3, 5, and 10, all of these complexes, with the exception of **6-MeOH** (Fig. 5) and **8-MeCN** (Fig. 10), were found to contain Fe in a five-coordinate, and thus coordinatively unsaturated environment, despite crystallization from coordinating solvents. With the exception of **6** (Fig. 5), those containing a Pr-linker (Fig. 3) were found to be approximately square pyramidal (τ-value = 0.01(**5**), 0.04(**7**), Table 1, highlighted in peach), and those containing an Et-linker were found to be approximately trigonal bipyramidal (τ-value = 0.60(**3**), 0.59(**4**); Table 1). Propyl-linked $([Fe^{II}(S\text{-}^{Me2}N_4(6\text{-H-DPPN})]^+$ (**6,** Fig. 5), which contains less sterically encumbering 6-H substituents, is closer to being ideal trigonal bipyramidal (τ-value = 0.81) than any of the other structures (Table 1). The Fe-S bonds of the complexes containing a propyl linker (**5** and **7**) are shorter than those containing an ethyl linker (**3** and **4**). These trends make sense given that the more orthogonal L-Fe-L' angles of a square pyramidal geometry provides better overlap with the metal ion d-orbitals. Square pyramidal $[Fe^{II}(S^{Me2}N_4(6\text{-Me-DPPN}))]^+$ (**5**) possesses the shortest Fe-S bond (2.3005(9) Å, Table 1), and trigonal bipyramidal

$[Fe^{II}(S^{Me2}N_4(quinoEN))]^+$ (**3**) and $[Fe^{II}(S^{Me2}N_4(6\text{-Me-DPEN})]^+$ (**4**), which contain the more sterically encumbering 6-Me or benzo substituents, possess the longest Fe-S bonds (2.3357(9) Å and 2.326(1) Å, respectively). In addition to steric interactions, poorer overlap between the sulfur and the metal ion d-orbitals in a trigonal bipyramidal geometry, are likely responsible for the longer Fe-S bonds in the latter. Metal-nitrogen bonds were similarly elongated in the trigonal bipyramidal complexes **3** and **4**. The average Fe-N bond length (Fe-N_{avg} = 2.12 Å) in primary amine-ligated $[Fe^{II}(S^{Me2}N_4(tren))]^+$ (**1**) is shorter than that of N^{Ar}-ligated **3**–**6**. This reflects the unfavorable steric interactions in the latter. Metal-nitrogen bonds were similarly elongated in the structurally analogous Mn(II) derivatives containing sterically encumbered *N*-heterocycles [52].

2.2. π-Accepting N^{Ar} ligands shift the electronic absorption bands into the visible region

Solutions of N^{Ar}/thiolate complexes **3** – **6** are all intensely colored and contain intense charge transfer bands in the visible region (λ_{max} = 387–502 nm) of the electronic absorption spectra (Figs. 6 and 7, and Figs. S4–S9), making it relatively easy to monitor reactivity (*vide infra*). This is in contrast to the primary amine complex, $[Fe^{II}(S^{Me2}N_4(tren))]^+$ (**1**), which is colorless, and only contains absorption bands in the UV region of the spectrum (λ_{max} = 290 nm) [48]. The energy of the lowest-energy band is sensitive to ring size, and red shifts when pyridine is replaced with a larger quinoline *N*-heterocycle, as was shown with previously reported π-donating/π-accepting thiolate/(α-imino)-*N*-heterocycle-ligated $\left[Fe^{II}(tame{-}N_2S(Me-Im)_2)\right]_2^{2+}$, $\left[Fe^{II}(tame{-}N_2S(py)_2)\right]_2^{2+}$ versus $\left[Fe^{II}(tame{-}N_2S(quino)_2)\right]_2^{2+}$ [8]. Although the λ_{max} of N^{Ar}/thiolate-ligated **3** (Fig. S4), **4** (Fig. S5), and **5** (Fig. S6) lie in the UV region of the spectrum, the intense ($\varepsilon \geq 1300\ cm^{-1}\ M^{-1}$) absorption bands are relatively broad and tail into the visible region to ~500 nm, resulting in an intense red or orange color.

2.3. Reversible solvent binding to Fe(II)-6

The electronic absorption spectra of the more sterically encumbered complexes **3**–**5**, and **7** (Scheme 1), are independent of solvent (Figs. S4–S8, Table S1), indicating that coordinating solvents do not bind to the open coordination site. The spectrum of the least sterically encumbered member of the series, **6**, on the other hand, is both solvent-dependent (Fig. 7) and temperature-dependent (Fig. 8, and Figs. S9 and S11, Tables S2–S4). This indicates that coordinating solvents (MeCN, MeOH, and THF) bind reversibly to the vacant site of **6**. Consistent with this, five-coordinate $[Fe^{II}(S^{Me2}N_4(6\text{-H-DPPN}))]^+$ (**6**, Fig. 5), could only be isolated from the non-coordinating solvent, CH_2Cl_2. Crystallization from MeOH affords a MeOH-bound derivative, $[Fe^{II}(S^{Me2}N_4(6\text{-H-DPPN}))\ (MeOH)]^+$ (**6-MeOH**, Fig. 5). The red-shift in λ_{max} (Figs. 7 and 8, Figs. S9, and S11) is consistent with the conversion of a 5- to 6-coordinate structure [6]. The Fe-O(1) bond length (Fig. 5, 2.210(2) Å), which is long relative to a typical methoxide Fe(II)-O bond (range: 1.864 Å–1.927 Å) [53,54], the H-bonding network in the crystal structure packing diagram, and the number of counterions, support the presence of a proton on O(1).

Temperature-dependent equilibrium constants (Tables S2–S4) for solvent binding to **6** were obtained via the quantitative addition of MeCN (Fig. S11), MeOH (Fig. 8), or THF (Fig. S9)

to five-coordinate **6** in CH_2Cl_2 over the temperature range 0 °C to −70 °C, and thermodynamic parameters for solvent binding (ΔH, ΔS) were obtained from a Van't Hoff plot (Fig. 9, Table 2, Figs. S10 and S12). Of the three solvents investigated, **6** has the highest affinity for MeOH $K_{eq}^{213K}(MeOH) = 26.7\ \underline{M}^{-1}$ versus $K_{eq}^{213K}(MeCN) = 0.70\ \underline{M}^{-1}$, and $K_{eq}^{213K}(THF) = 1.33\ \underline{M}^{-1}$), with an associated enthalpy (ΔH) that is approximately twice that of MeCN and THF (Table 2). The negative entropy parameters (ΔS) are consistent with an associative process.

Aside from *N*-heterocycle-ligated **6**, $[Fe^{II}(S^{Me2}N_4(6\text{-H-DPEN}))(\mu\text{-}S^{Me2}N_4(6\text{-H-DPEN})Fe^{II}(MeCN)](PF_6)_2$ (**8**) is the only other thiolate-ligated ferrous complex synthesized by our group that readily binds neutral ligands (i.e., solvents, Fig. S13). Complex **8** contains an Et-linker in place of the Pr-linker of **6**, and an unencumbering 6-H substituent, and was crystallized from MeCN. As shown in the ORTEP diagram of Fig. 10, both Fe(II) ions are six-coordinate: Fe(2) contains a MeCN coordinated to the sixth coordination site, and Fe(1) contains a thiolate provided by the adjacent Fe(2) in the sixth coordination site. This implies that the Fe(II) ion of both **8** and **6** is either more accessible (a steric effect), or more Lewis acidic (an electronic effect) relative to the other complexes described herein (*vide infra*). Previously we showed that electron-rich π-donating thiolate ligands decrease metal ion Lewis acidity in primary amine-ligated Fe(II) complexes favoring coordinatively unsaturated structures [27,30,55]. The greater affinity that **6** and **8** have for additional ligands can therefore be attributed to the π-accepting properties of the pyridine partially off-setting the π-donor properties of the thiolate, as well as the 6-H substituents creating more space for incoming ligands. Comparison of the space-filling diagrams of **3**, **4**, **5**, and **6** in Fig. 11 shows that metal ion accessibility not only depends on steric bulk (e.g., **3** and **4**) but also the geometry of the complex. The metal ion is most visible, and thus most accessible, in trigonal bipyramidal **6**, and least accessible in square pyramidal **5**, and this influences reactivity with substrates such as O_2. Although **8** (Fig. 10) is dimeric in the solid state, magnetic susceptibility data (Fig. S14) indicates that the dimer cleaves to form monomers in coordinating solvents. In MeOH, the magnetic moment (μ_{eff} = 4.92 BM at 298 K), determined using thse Evan's method, indicates that **8-MeOH** is monomeric and high-spin, $S = 2$. Confirmation of this was obtained using high resolution linear trap quadropole (LTQ) Orbitrap mass spectroscopy, which shows isotopomers differing by single, as opposed to half mass, units (Fig. S15). The detected peak at 428.13 m/z (M + 31) matches the calculated mass for a six-coordinate methanol-bound complex, $[Fe^{II}(S^{Me2}N_4(6\text{-H-DPEN}))(MeOH)]^+$ (**8-MeOH**). In MeCN, the high resolution LTQ ion trap mass spectrum of **8** shows isotopomers that differ both by half mass units, as well as single mass units (Fig. S16), indicating that an equilibrium mixture (Fig. S17) of dicationic dimer and monocationic monomers exists in this solvent. The ratio of $\mu_{eff}^2(expt)/\mu_{eff}^2(theoretical)$ provides the percentage of monomeric species **8-MeCN** in solution at a given temperature (52.3% at 298 K, Fig. S17) [8].

2.4. Anion binding

Although neutral solvent molecules were found only to bind to the least sterically hindered members of the series, **6** and **8**, anionic ligands, such as OAc^- and N_3^-, on the other hand,

were shown to bind even to some of the more sterically hindered members of the series. For example, $Bu_4N(N_3)$ (Figs. S18 and S19) and acetate (Fig. 12 and Fig. S20) were shown to bind to **3** and **4**. Azide was also shown to bind to **8** (Fig. S21). The red-shift in λ_{max} (from e.g., 474 nm to 554 nm for N_3^- binding to **8**) caused by anion binding would suggest that the bands involve a Fe(d) → **π***(*N*-heterocycle) charge transfer transition, analogous to what we previously observed [8]. The ability to detect anion binding to Fe(II) contrasts with primary amine-ligated [Fe(II) (trenS)]$^+$ (**1**) and bodes well for our goal of probing superoxide ($O_2^{\bullet -}$) binding to Fe(II). Reactivity with the $O_2^{\bullet -}$ will be the subject of a separate manuscript.

2.5. Oxidation potentials as a probe of metal ion Lewis acidity

In order to promote superoxide reduction and/or oxidation, a transition-metal complex must be stable in multiple oxidation states. Redox potentials not only provide information about the relative stability of two oxidation states, but also provide a quantitative measure of metal ion Lewis acidity. As shown by the redox potentials in Table 3, and the cyclic voltammograms of Fig. 13 and Figs. S22–S26, **π**-accepting *N*-heterocycles increase metal ion Lewis acidity relative to the primary amines of [$Fe^{II}(S^{Me2}N_4$(tren))]$^+$ (**1,** −150 mV vs SCE), as we had anticipated. This is shown by the more positive potential at which Fe(II) converts to Fe(III) ($E_{p,a}$) for complexes **3**–**7**, and **8**, relative to that of **1** (Table 3), which shifts by as much as 585 mV. Given that redox potentials reflect the relative stability of two different oxidations states, the higher potential for complexes **3**–**7** and **8** indicate that **π**-accepting *N*-heterocycles make the complexes are more difficult to oxidize, and cause the highest occupied molecular orbitals (HOMOs) to lie lower in energy for the *N*-heterocycle amine-ligated complexes. The potentials associated with 6-coordinate **6-MeOH** and **8-MeCN** shift less than the others (by as little as +191 mV), relative to **1** reflecting an increase in electron density at the metal caused by the sixth ligand. The lower potential for these complexes also reflects the increased stability of Fe(III) in its preferred six-coordinate environment. The chemical irreversibility of waves associated with the Fe(II)/Fe(III) couple of complexes **3**–**7** (Figs. S22–S24, and S26–S27) indicates that the five-coordinate structures convert to six-coordinate structures upon oxidation, as observed previously by our group [56]. The reversible wave associated with the **8-MeCN**/**8^{ox}-MeCN** couple (Fig. 13), as well as the **6-MeOH**/**6^{ox}-MeOH** (Fig. S25) reflects the fact that, unlike the other complexes, **8-MeCN** and **6-MeOH** are six-coordinate to begin with.

2.6. Outer sphere oxidation

Although too unstable to isolate, *in situ* formation of oxidized Fe(III) derivatives via the addition of either (p-tolyliminium)PF_6 or $(Cp_2Fe)PF_6$, depending on the redox potential, could be monitored by electronic absorption spectroscopy (Fig. 14, and Figs. S27–S29). As illustrated in Fig. 14 for **8-MeCN**, the absorption bands associated with the Fe(II) derivative disappear upon oxidation and are replaced with new absorption bands in the ~600 nm region of the spectrum. The observed red-shift would be more consistent with a LMCT transition, than a MLCT transition, being responsible for the new absorption features, given that the metal ion orbitals would drop in energy. The rhombic ⊥-mode EPR signals at g = 2.180, 2.145, 2.008 (Fig. 15), and g = 2.25, 2.17, 1.98 (Fig. S30), for **8^{ox}-MeCN** and **6^{ox}-MeOH,** respectively, indicate that the oxidized ferric products are monomeric and low-spin (*S* = 1/2).

2.7. Dioxygen reactivity

The addition of dry O_2 to complexes **3**, **4**, **6**, **7**, and **8** at ambient temperatures in CH_2Cl_2 causes the orange/red solutions to become intensely purple in color. This color change is accompanied by the growth of a band in the electronic absorption spectrum in the range 494 – 587 nm (Fig. 16 and Figs. S31–S33). The λ_{max} is dependent on both the *N*-heterocycle and its substituent. These bands are red-shifted relative to that of primary amine-ligated $[Fe^{III}(S^{Me2}N_4(tren))]_2(\mu\text{-oxo})^+$ (**9**) (λ_{max} = 485 nm), reflecting the greater Lewis acidity of the metal ions of **3**, **4**, **6**, **7**, and **8**, due to the incorporation of π-accepting *N*-heterocycle ligands. The rate at which purple dioxygen products form is dependent on the redox potential of the Fe(II) precursor, and thus the metal ion Lewis acidity. For example, the rate at which the dioxygen product of **8-MeOH** ($E_{1/2}$ = −90 mV,$E_{p,a}$ = −60 mV vs SCE, Fig. 13) forms ($k_{obs}^{200K} = 2.4 \times 10^{-2}\ s^{-1}$, $t_{1/2}$ = 29 *sec*, Fig. S34) is significantly faster than the rate at which the dioxygen product of both **3** ($E_{p,a}$ = +439 mV vs SCE, Fig. S22) and **4** ($E_{p,a}$ = +449 mV vs SCE, Fig. S23) forms ($k_{obs}^{298K}(3) = 4.9 \times 10^{-3}\ s^{-1}$, $t_{1/2}$(**3**) = 141 *sec*, Fig. 17); $k_{obs}^{298K}(4) = 2.3 \times 10^{-3}\ s^{-1}$, $t_{1/2}$(**4**) = 301 *sec*, Fig. S35), and the latter two are at a higher temperature. In contrast to all of the other Fe(II) complexes discussed herein, complex **5** ($E_{p,a}$ = +486 mV vs SCE, Fig. S24) does not react with O_2 at all, even with prolonged reaction times (48 hr). This likely reflects the more sterically congested, less accessible Fe site of **5** (Fig. 11). As shown in the ORTEP diagrams of Fig. 18, and Figs. S36–S38, the structure of the purple product, $\mathbf{3^{\mu\text{-}oxo}}$, $\mathbf{4^{\mu\text{-}oxo}}$, $\mathbf{6^{\mu\text{-}oxo}}$, and $\mathbf{8^{\mu\text{-}oxo}}$, is analogous to primary amine-ligated **9** [57], and contains a single unsupported oxo atom bridging between two ferric ions. There is a direct correlation between the λ_{max} of the absorption band associated with the mono oxo-bridged products, and the $Fe\cdots N^{Ar}$ distance (Fig. 19), and an inverse correlation between oxidation potential, $E_{p,a}$, and λ_{max} (Fig. 20). These trends can be explained based on the expected drop in the energy of metal ion d-orbitals expected with an increase in metal ion Lewis acidity. The less sterically encumbered complexes, $\mathbf{6^{\mu\text{-}oxo}}$ and $\mathbf{8^{\mu\text{-}oxo}}$, with R = H substituents possess the shorter Fe-N^{Ar} bonds, and this increases electron density at the metal ion, thus decreasing metal ion Lewis acidity. If the absorption bands involve LMCT transitions, then for the reasons outlined above, one would expect the band to shift to lower energies, or higher wavelength, as metal ion Lewis acidity increases, as seen in Fig. 19. The absorption band, λ_{max}, of the least sterically hindered (R = H) oxo, $\mathbf{8^{\mu\text{-}oxo}}$, with the shortest Fe-$N^{Ar}$ bonds is closest in energy to that of primary amine-ligated **1**. In contrast to the dioxygen chemistry of the corresponding Mn(II) derivatives, where as many as four metastable intermediates are observed [49,50,58], no intermediates are observed *en route* to our mono oxo-bridged Fe products, $\mathbf{3^{\mu\text{-}oxo}}$, $\mathbf{4^{\mu\text{-}oxo}}$, $\mathbf{6^{\mu\text{-}oxo}}$, and $\mathbf{8^{\mu\text{-}oxo}}$. This implies that with Fe(II), either O_2 binding is rate-determining, or the iron-dioxygen intermediates are less stable than our manganese-dioxygen intermediates. Both could be due to the fact that Fe(II) contains an additional destabilizing antibonding electron. Selected metrical parameters of mono oxo bridged $\mathbf{3^{\mu\text{-}oxo}}$, $\mathbf{4^{\mu\text{-}oxo}}$, $\mathbf{6^{\mu\text{-}oxo}}$, and $\mathbf{8^{\mu\text{-}oxo}}$ are shown in Table 4. As shown previously with the mono oxo-bridged Mn(III)-analogues, $Fe\cdots N^{Ar}$ distances (Fe-$N(3,4)_{avg}$ = 2.34 Å for $\mathbf{3^{\mu\text{-}oxo}}$, and Fe-$N(3,4)_{avg}$ = 2.41 Å for $\mathbf{4^{\mu\text{-}oxo}}$) of the complexes containing encumbering substituents on the *N*-heterocycle, $\mathbf{3^{\mu\text{-}oxo}}$ and $\mathbf{4^{\mu\text{-}oxo}}$, are significantly longer than the sum of their covalent radii (2.11 Å) [59]. This supports our earlier conclusions [52],

suggesting that ligand constraints, as opposed to Jahn-Teller-like effects expected for high-spin d^4-transition-metals [49], is responsible for the longer bonds in our mono oxo-bridged M(III) (M = Mn, Fe) complexes.

Mono oxo-bridged μ-oxo Fe dimers are typically unreactive and quite stable under most conditions [60]. However, we previously showed that proton-induced cleavage of the oxo-bridge of $[Fe^{III}(S^{Me2}N_4(tren))]_2(\mu\text{-}O)^{2+}$ (**9**) occurs when an electron-donating thiolate is included in the coordination sphere [57]. We hypothesized that this was because the thiolate creates a more basic oxo was, which is more susceptible to protonation. In the current study, we find that even when **π**-accepting ligands are incorporated into the coordination sphere, the oxo is basic enough to undergo proton-induced cleavage. For example, HOAc reacts with $\mathbf{4^{\mu\text{-}oxo}}$ in MeCN to afford a species with a red-shifted λ_{max} at 630 nm (Fig. 21). This spectrum is different from the (p-tolyliminium)PF_6 oxidized product derived from **4** (Figure S28). The former (Fig. 19) presumably contains an acetate coordinated to the sixth coordination site, analogous to the crystallographically characterized product derived from **9** [57,61], whereas (p-tolyliminium)PF_6 oxidized $\mathbf{4^{ox}}$ presumably has a coordinated MeCN in the coordination sphere, given the preference that Fe(III) has for being six-coordinate. All of the ferric derivatives examined in the current study were too unstable to isolate, with the exception of the mono oxo-bridged dimers. The instability of ferric complexes containing **π**-accepting *N*-heterocycle ligands (Fig. 4) reflect their higher redox potentials (Figs. S22–S26), and thus greater metal ion Lewis acidity, of the complexes discussed herein.

3. Summary and conclusions

This work shows that metal ion Lewis acidity can be modulated by including **π**-accepting ligands in the coordination sphere, or, by increasing steric bulk and constraining both ligand geometry as well as $Fe\cdots N^{Ar}$ distances, especially in oxidized Fe(III)-derivatives. Ferrous, Fe (II) complexes containing more Lewis acidic metal ions have charge transfer bands in the visible region of the electronic absorption spectrum, and a higher affinity for a sixth ligand. This is in contrast to our previously reported primary amine-ligated complex, **1**, which mimics superoxide reductase (SOR) function. The higher energy charge transfer transition associated with **1** made it difficult to visualize substrate-bound Fe(II) derivatives, and thus we were unable to distinguish between a concerted versus step-wise mechanism in the oxidative addition of HO_2 (Fig. 1). Neutral ligands were shown to bind reversibly to the least sterically encumbered complexes, and anionic ligands were shown to bind to all of the complexes reported herein. Thermodynamic parameters associated with the former were obtained from temperature-dependent equilibrium constants. With the exception of the most sterically encumbered complex (Fig. 11), all of the complexes described herein were shown to react with O_2, with rates dependent on oxidation potential, $E_{p,a}$ indicating that an electron transfer event takes place. In contrast to our previously reported Mn(II) derivatives [49,52], dioxygen intermediates are not observed with the Fe(II) complexes reported herein.

Supplementary Material

Refer to Web version on PubMed Central for supplementary material.

Acknowledgment

This work was supported by NIH grants RO1-GM45881 and R01-GM123062.

References

[1]. Blakely MN, Dedushko MA, Poon PCY, Villar-Acevedo G, Kovacs JA, Formation of a reactive, alkyl thiolate-ligated FeIII-superoxo intermediate derived from dioxygen, J. Am. Chem. Soc 141 (2019) 1867–1870. [PubMed: 30661357]

[2]. Poon PCY, Dedushko MA, Sun X, Yang G, Toledo S, Hayes EC, Johansen A, Rees JA, Stoll S, Rybek-Akimova E, Kovacs JA, How metal ion Lewis acidity and steric properties influence the barrier to dioxygen binding, peroxo O-O bond cleavage, and reactivity, J. Am. Chem. Soc 141 (2019) 15046–15057, 10.1021/jacs.9b04729. [PubMed: 31480847]

[3]. Tamanaha EY, Zhang B, Guo Y, Chang W-C, Bollinger JM Jr., Krebs C,, Spectroscopic evidence for the two C-H-cleaving intermediates of Aspergillus nidulans isopenicillin N synthase, J. Am. Chem. Soc 138 (2016) 8862–8874. [PubMed: 27193226]

[4]. Green MT, C-H bond activation in heme proteins: the role of thiolate ligation in cytochrome P450, Curr. Op. Chem. Biol 13 (2009) 84–88.

[5]. Groves JT, Using push to get pull, Nature Chem. 6 (2014) 89–91. [PubMed: 24451580]

[6]. Kennepohl P, Neese F, Schweitzer D, Jackson HL, Kovacs JA, Solomon EI, Spectroscopy of non-Heme iron thiolate complexes: insight into the electronic structure of the Low-spin active site of nitrile hydratase, Inorg. Chem 44 (2005) 1826–1836. [PubMed: 15762709]

[7]. Lugo-Mas P, Dey A, Xu L, Davin SD, Benedict J, Kaminsky W, Hodgson KO, Hedman B, Solomon EI, Kovacs JA, How does single oxygen atom addition affect the properties of an Fe-nitrile hydratase analogue? The compensatory role of the unmodified thiolate, J. Am. Chem. Soc 128 (2006) 11211–11221. [PubMed: 16925440]

[8]. Leipzig B, Rees J, Kawalska JK, Theisen RM, Kavcic M, Poon PCY, Kaminsky W, DeBeer S, Bill E, Kovacs JA, How do ring size and π-donating thiolate ligands affect redox-Active, α-imino-N-heterocycle ligand activation? Inorg. Chem 57 (2018) 1935–1949. [PubMed: 29411979]

[9]. Kitajima N, Fujisawa K, Tanaka M, Moro-oka Y, X-ray Structure of thiolatocopper(II) complexes bearing close spectroscopic similarities to blue copper proteins, J. Am. Chem. Soc 114 (1992) 9232–9233.

[10]. Solomon EI, Szilagyi RK, DeBeer George S, Basumallick L, Electronic structures of metal sites in proteins and models: contributions to function in blue copper proteins, Chem. Rev 104 (2004) 419–458. [PubMed: 14871131]

[11]. Sahu S, Goldberg DP, Activation of dioxygen by iron and manganese complexes: a heme and nonheme perspective, J. Am. Chem. Soc 138 (2016) 11410–11428. [PubMed: 27576170]

[12]. Burzlaff NI, Rutledge PJ, Clifton IJ, Hensgens CMH, Pickford M, Adlington RM, Roach PL, Baldwin JE, The reaction cycle of isopenicillin N synthase observed by X-ray diffraction, Nature 401 (1999) 721–724. [PubMed: 10537113]

[13]. Brown CD, Neidig ML, Neibergall MB, Lipscomb JD, Solomon EI, VTVHMCD and DFT studies of thiolate bonding to {FeNO}7/{FeO2}8 complexes of isopenicillin N synthase: substrate determination of oxidase versus oxygenase activity in nonheme Fe enzymes, J. Am. Chem. Soc 129 (23) (2007) 7427–7438. [PubMed: 17506560]

[14]. Kovacs JA, Brines LM, Understanding how the thiolate sulfur contributes to the function of the non-heme iron enzyme superoxide reductase, Acc. Chem. Res 40 (7) (2007) 501–509. [PubMed: 17536780]

[15]. Kitagawa T, Dey A, Lugo-Mas P, Benedict J, Kaminsky W, Solomon E, Kovacs JA, A functional model for the metalloenzyme superoxide reductase, J. Am. Chem. Soc 128 (2006) 14448–14449. [PubMed: 17090014]

[16]. Clay MD, Cosper CA, Jenney FE, Adams MWW, Johnson MK, Nitric oxide binding at the mononuclear active site of reduced Pyrococcus furiosus superoxide reductase, Proc. Natl. Acad. Sci. U.S.A 100 (7) (2003) 3796–3801. [PubMed: 12655067]

[17]. Shearer J, Scarrow RC, Kovacs JA, Synthetic models for the cysteinate-ligated non-heme iron enzyme superoxide reductase: observation and structural characterization by XAS of an Fe(III)-OOH intermediate, J. Am. Chem. Soc 124 (39) (2002) 11709–11717. [PubMed: 12296737]

[18]. Yeh AP, Hu Y, Jenney FE Jr., Adams MWW, Rees DC, Structures of the superoxide reductase from Pyrococcus furiosus in the oxidized and reduced states, Biochemistry 39 (10) (2000) 2499–2508. [PubMed: 10704199]

[19]. Emerson JP, Coulter ED, Cabelli DE, Phillips RS, Kurtz DM Jr., Kinetics and mechanism of superoxide reduction by two-iron superoxide reductase from DesulfoVibrio Vulgaris, Biochemistry 41 (2002) 4348–4357. [PubMed: 11914081]

[20]. Blaesi EJ, Fox BG, Brunold TC, Spectroscopic and computational investigation of iron(III) Cysteine Dioxygenase: Implications for the nature of the putative superoxo-Fe(III) intermediate, Biochemistry 53 (2014) 5759–5770. [PubMed: 25093959]

[21]. Kumar D, Thiel W, de Visser SP, Theoretical study on the mechanism of the oxygen activation process in cysteine dioxygenase enzymes, J. Am. Chem. Soc 133 (2011) 3869–3882. [PubMed: 21344861]

[22]. Gardner JD, Pierce BS, Fox BG, Brunold TC, Spectroscopic and computational characterization of substrate-bound mouse cysteine dioxygenase: nature of the ferrous and ferric cysteine adducts and mechanistic implications, Biochemistry 49 (2010) 6033–6041. [PubMed: 20397631]

[23]. Aluri S, Visser SP, The mechanism of cysteine oxygenation by cysteine dioxygenase enzymes, J. Am. Chem. Soc 129 (48) (2007) 14846–14847. [PubMed: 17994747]

[24]. Jeschke J, O'Hagan HM, Zhang W, Vatapalli R, Freitas Calmon M, Danilova L, Nelkenbrecher C, Van Neste L, Bijsmans ITGW, Van Engeland M, Gabrielson E, Schuebel KE, Winterpach A, Baylin SB, Herman JG, Ahuja N, Frequent inactivation of cysteine dioxygenase type 1 contributes to survival of breast cancer cells and resistance to anthracyclines, Clin. Cancer Res 19 (2013) 3201–3211. [PubMed: 23630167]

[25]. Kwon J, Park M, Kim J-H, Lee HW, Kang MC, Park JH, Epigenetic regulation of the novel tumor suppressor cysteine dioxygenase 1 in esophageal squamous cell carcinoma, Tumour Biol. 36 (10) (2015) 7449–7456. [PubMed: 25903467]

[26]. Li W, Pierce BS, Steady-state substrate specificity and O2-coupling efficiency of mouse cysteine dioxygenase, Arch. Biochem. Biophys 565 (2015) 49–56. [PubMed: 25444857]

[27]. Kovacs JA, Synthetic analogues of cysteinate-ligated non-heme iron, and noncorrinoid cobalt enzymes, Chem. Rev 104 (2004) 825–848. [PubMed: 14871143]

[28]. Brennan BA, Jin H, Chase DB, Turner IM, Buck C, Scarrow RC, Gurbiel R, Doan P, Hoffman BM, Nelson MJ, Nitrile hydratase: a novel iron-sulfur center, J. Inorg. Biochem 51 (1993) 374.

[29]. Huang W, Jia J, Cummings J, Nelson M, Schneider G, Lindqvist Y, Crystal structure of nitrile hydratase reveals a novel iron centre in a novel fold, Structure 5 (1997) 691–699. [PubMed: 9195885]

[30]. Ellison JJ, Nienstedt A, Shoner SC, Barnhart D, Cowen JA, Kovacs JA, Reactivity of five-coordinate models for the thiolate-ligated Fe site of nitrile hydratase, J. Am. Chem. Soc 120 (23) (1998) 5691–5700.

[31]. Yamanaka Y, Kato Y, Hashimoto K, Iida K, Nagasawa K, Nakayama H, Dohmae N, Noguchi K, Noguchi T, Yohda M, Odaka M, Time-resolved crystallography of the reaction intermediate of nitrile hydratase: revealing a role for the cysteinesulfenic acid ligand as a catalytic nucleophile, Angew. Chem lnt. Ed 54 (2015) 10763–10767.

[32]. Krest CM, Silakov A, Rittle J, Yosco TH, Onderko EL, Calixto JC, Green MT, Significantly shorter Fe–S bond in cytochrome P450-I is consistent with greater reactivity relative to chloroperoxidase, Nature Chem. 7 (2015) 696–702. [PubMed: 26291940]

[33]. Yosca TH, Rittle J, Krest CM, Oderko EL, Silakov A, Calixto JC, Behan RK, Green MT, Iron(IV)hydroxide pKa and the role of thiolate ligation in C-H bond activation by cytochrome P450, Science 342 (2013) 825–829. [PubMed: 24233717]

[34]. Rittle J, Green MT, Cytochrome P450 compound I: capture, characterization, and C-H bond activation, Science 330 (2010) 933–937. [PubMed: 21071661]

[35]. Cook SA, Borovik AS, Molecular designs for controlling the local environments around metal ions, Acc. Chem. Res 48 (2015) 2407–2414. [PubMed: 26181849]

[36]. Cook SA, Hill EA, Borovik AS, Lessons from nature: a bio-inspired approach to molecular design, Biochemistry 54 (2015) 4167–4180. [PubMed: 26079379]

[37]. Shirin Z, Hammes BS, Young VG, Borovik AS, Hydrogen Bonding in metal oxo complexes: synthesis and structure of a monomeric manganese(III)-oxo complex and its hydroxo analogue, J. Am. Chem. Soc 122 (2000) 1836–1837.

[38]. Borovik AS, Bioinspired hydrogen bond motifs in ligand design: the role of noncovalent interactions in metal ion mediated activation of dioxygen, Acc. Chem. Res 38 (2005) 54–61. [PubMed: 15654737]

[39]. Kovacs JA, How iron activates O2, Science 299 (2003) 1024–1025. [PubMed: 12586930]

[40]. Bell SR, Groves JT, A highly reactive P450 model compound I, J. Am. Chem. Soc 131 (2009) 9640–9641. [PubMed: 19552441]

[41]. Shoner S, Barnhart D, Kovacs JA, A Model for the low-spin, non-heme, thiolate-ligated iron site of nitrile hydratase, Inorg. Chem 34 (1995) 4517–4518.

[42]. Jackson HL, Shoner SC, Rittenberg D, Cowen JA, Lovell S, Barnhart D, Kovacs JA, Probing the influence of local coordination environment on the properties of Fe-type nitrile hydratase model complexes, Inorg. Chem 40 (7) (2001) 1646–1653. [PubMed: 11261975]

[43]. Shearer J, Kung IY, Lovell S, Kaminsky W, Kovacs JA, Why is there an “Inert” metal center in the active site of nitrile hydratase? reactivity and ligand dissociation from a five-coordinate Co(III) nitrile hydratase model, J. Am. Chem. Soc 123 (3) (2001) 463–468. [PubMed: 11456548]

[44]. Shearer J, Jackson HL, Schweitzer D, Rittenberg DK, Leavy TM, Kaminsky W, Scarrow RC, Kovacs JA, The first example of a nitrile hydratase model complex that reversibly binds nitriles, J. Am. Chem. Soc 124 (2002) 11417–11428. [PubMed: 12236756]

[45]. Shearer J, Scarrow RC, Kovacs JA, Synthetic models for the cysteinate–ligated non-heme iron enzyme superoxide reductase: observation and structural characterization by XAS of an FeIII–OOH Intermediate, J. Am. Chem. Soc 124 (2002) 11709–11717. [PubMed: 12296737]

[46]. Kurtz DM, Coulter ED, The mechanism(s) of superoxide reduction by superoxide reductases in vitro and in vivo, J. Biol. Inorg. Chem 7 (2002) 653–658. [PubMed: 12072973]

[47]. Clay MD, Jenney FE Jr., Hagedoorn PL, George GN, Adams MWW, Johnson MK, Spectroscopic studies of pyrococcus furiosus superoxide reductase: implications for active-site stuctures and the catalytic mechanism, J. Am. Chem. Soc 124 (2002) 788–805. [PubMed: 11817955]

[48]. Shearer J, Nehring J, Kaminsky W, Kovacs JA, Modeling the reactivity of superoxide reducing metalloenzymes with a nitrogen and sulfur coordinated iron complex, Inorg. Chem 40 (2001) 5483–5484. [PubMed: 11599942]

[49]. Poon PCY, Dedushko MA, Sun X, Yang G, Toledo S, Hayes EC, Johansen A, Piquette MC, Rees JA, Stoll S, Rybek-Akimova E, Kovacs JA, How metal ion lewis acidity and steric properties influence the barrier to dioxygen binding, peroxo O-O bond cleavage, and reactivity, J. Am. Chem. Soc 141 (38) (2019) 15046–15057. [PubMed: 31480847]

[50]. Coggins MK, Sun X, Kwak Y, Solomon EI, Rybak-Akimova E, Kovacs JA, Characterization of metastable intermediates formed in the reaction between a Mn (II) complex and dioxygen, including a crystallographic structure of a binuclear Mn (III)-peroxo species, J. Am. Chem. Soc 135 (2013) 5631–5640. [PubMed: 23470101]

[51]. Toledo S, Downing AN, Kaminsky W, Kovacs JA, Synthesis and structure of thiolate-ligated fe complexes containing a **π**-accepting pyridine ligand scaffold. 2021, Manuscript in preparation.

[52]. Coggins MK, Toledo S, Shaffer E, Kaminsky W, Shearer J, Kovacs JA, Characterization and dioxygen reactivity of a new series of coordinatively unsaturated thiolate-ligated manganese(II) complexes, Inorg. Chem 51 (12) (2012) 6633–6644. [PubMed: 22642272]

[53]. Pascualini ME, Stoian SA, Ozarowski A, Abboud KA, Veige AS, Solid state collapse of a high-spin square-planar Fe(II) complex, solution phase dynamics, and electronic structure characterization of an Fe(II)2 dimer, Inorg. Chem 55 (2016) 5191–5200. [PubMed: 27182796]

[54]. Chambers MB, Groysman S, Villagran D, Nocera DG, Iron in a trigonal tris (alkoxide) ligand environment, Inorg. Chem 52 (2013) 3159–3169. [PubMed: 23432161]

[55]. Lugo-Mas P, Taylor W, Schweitzer D, Theisen RM, Xu L, Shearer J, Swartz RD, Gleaves MC, DiPasquale A, Kaminsky W, Kovacs JA, Properties of square-pyramidal alkyl thiolate FeIII

complexes, including an analogue of the unmodified form of nitrile hydratase, Inorg. Chem 47 (2008) 11228–11236. [PubMed: 18989922]

[56]. Swartz RD, Coggins MK, Kaminsky W, Kovacs JA, Nitrile Hydration by thiolate– and alkoxide-ligated Co-NHase analogues. isolation of Co(III)-amidate and Co(III)–iminol intermediates, J. Am. Chem. Soc 133 (2011) 3954–3963. [PubMed: 21351789]

[57]. Theisen RM, Shearer J, Kaminsky W, Kovacs JA, Steric and electronic control over the reactivity of a thiolate-ligated Fe(II) complex with dioxygen and superoxide. Reversible mu-oxo dimer formation, Inorg. Chem 43 (2004) 7682–7690. [PubMed: 15554633]

[58]. Kovacs JA, Tuning the relative stability and reactivity of manganese dioxygen and Peroxo intermediates via systematic ligand modification, Acc. Chem. Res 48 (2015) 2744–2753. [PubMed: 26335158]

[59]. Shannon RD, Revised effective ionic radii and systematic studies of interatomie distances in halides and chaleogenides, Acta. Cryst. A32 (1976) 751–767.

[60]. Kurtz DM Jr., Oxo- and hydroxo-bridged Diiron complexes: a chemical perspective on a biological unit, Chem. Rev 90 (1990) 585–606.

[61]. Shearer J, Fitch SB, Kaminsky W, Benedict J, Scarrow RC, Kovacs JA, How does cyanide inhibit superoxide reductase? Insight from synthetic FeIIIN4S model complexes, Proc. Natl. Acad. Sci 100 (2003) 3671–3676. [PubMed: 12655068]

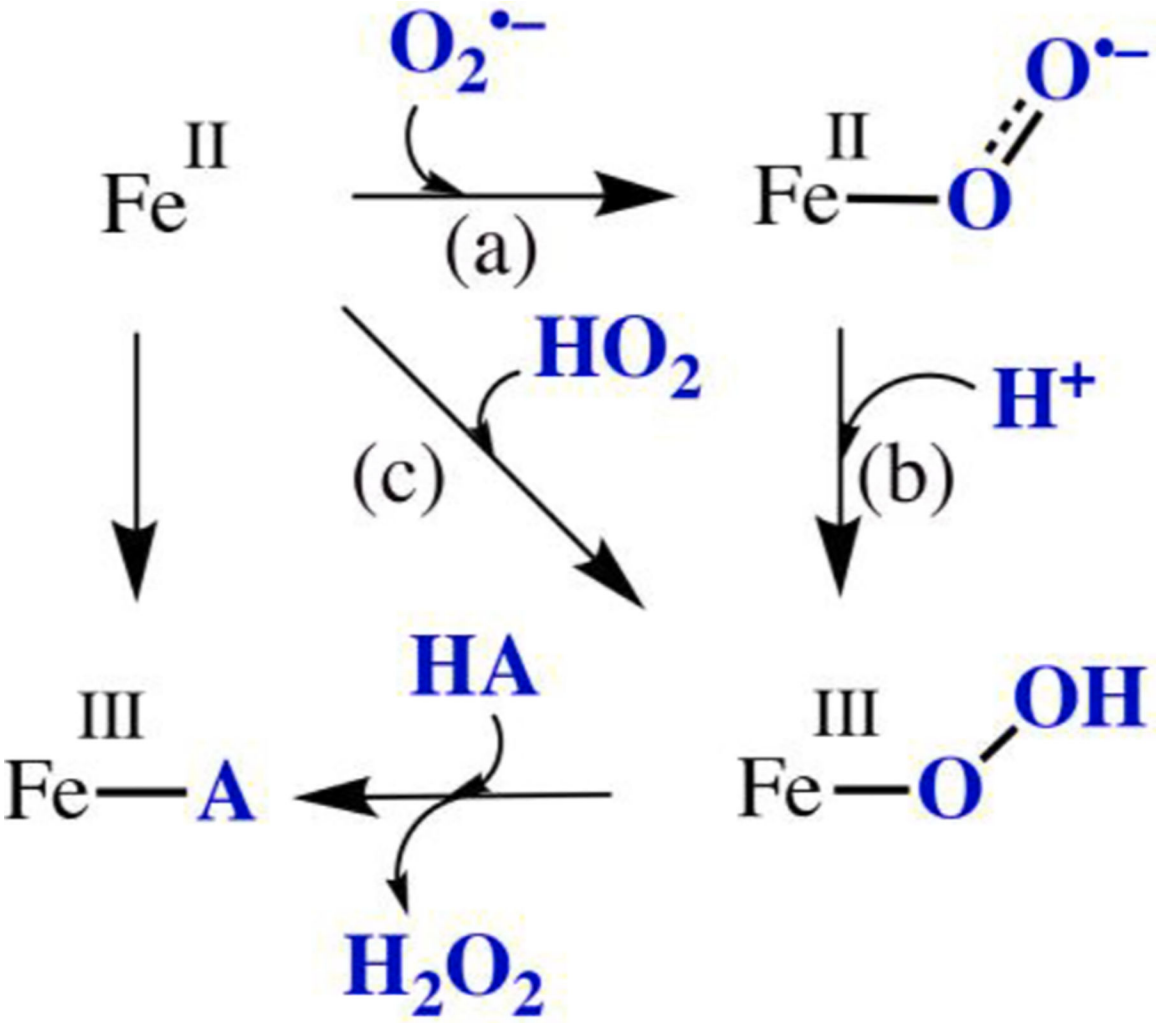

Fig. 1.
Sequential, (a) + (b), versus concerted, (c), addition of HO_2 to Fe(II) to afford an Fe(III)–OOH.

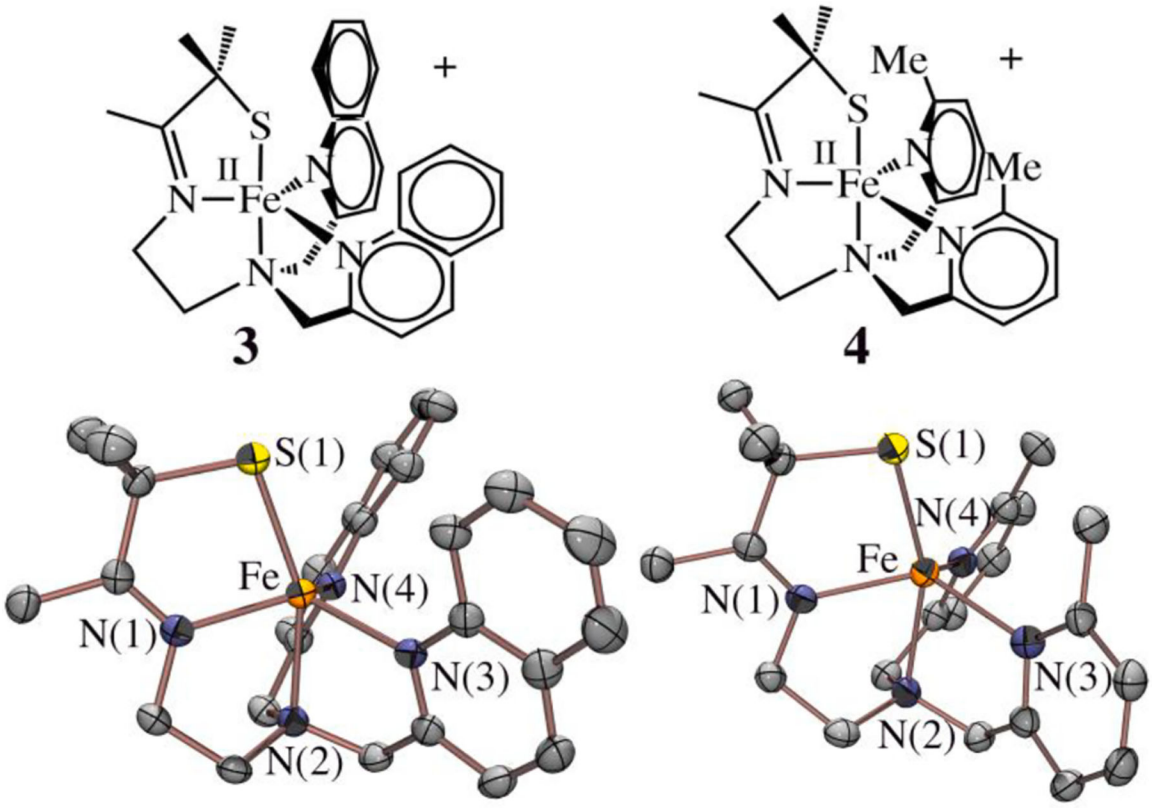

Fig. 2.

ORTEP diagrams of coordinatively unsaturated thiolate-ligated **3** and **4**. Hydrogen atoms, counterions, and cosolvents have been removed, and chemdrawings included for clarity.

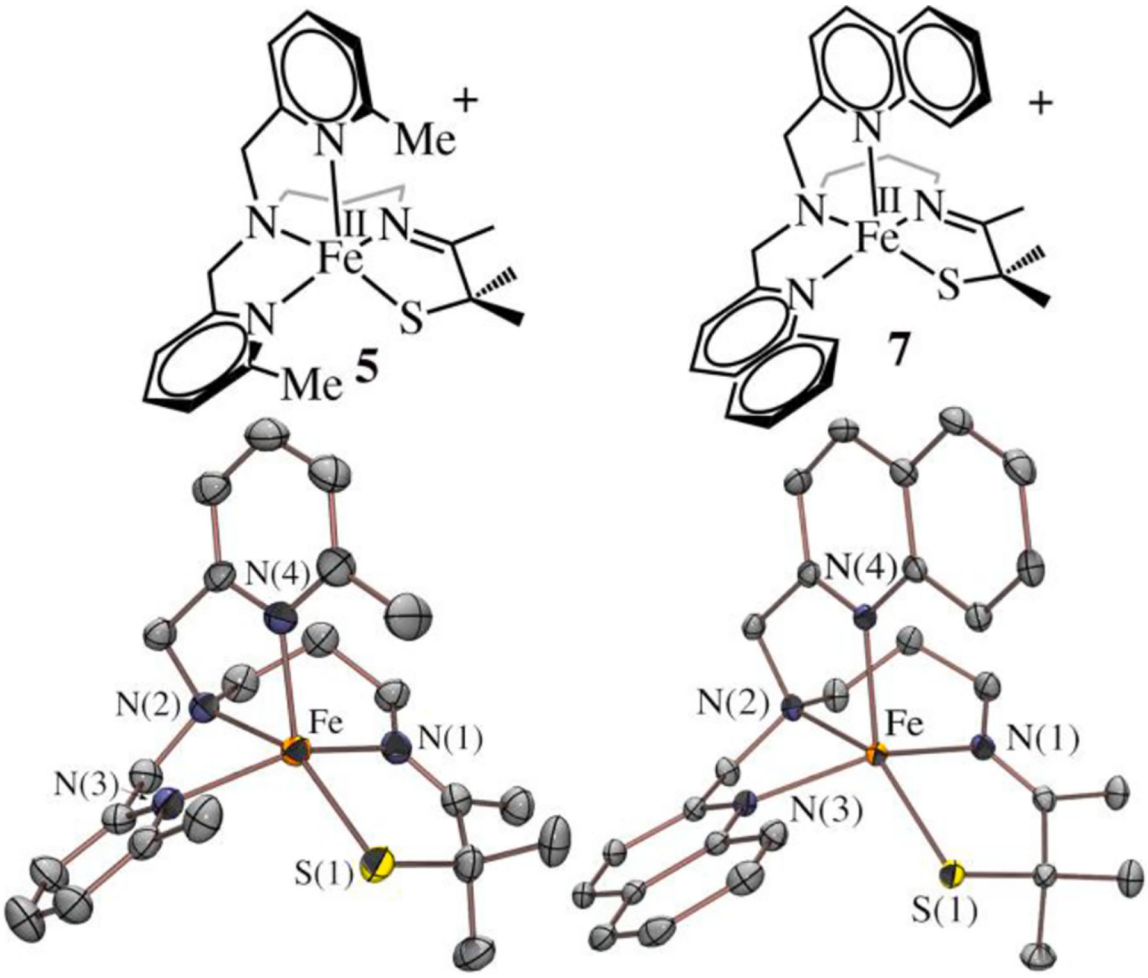

Fig. 3.

ORTEP diagrams of coordinatively unsaturated thiolate-ligated **5** and **7**. Hydrogen atoms, counterions, and cosolvents have been removed, and chemdrawings included for clarity.

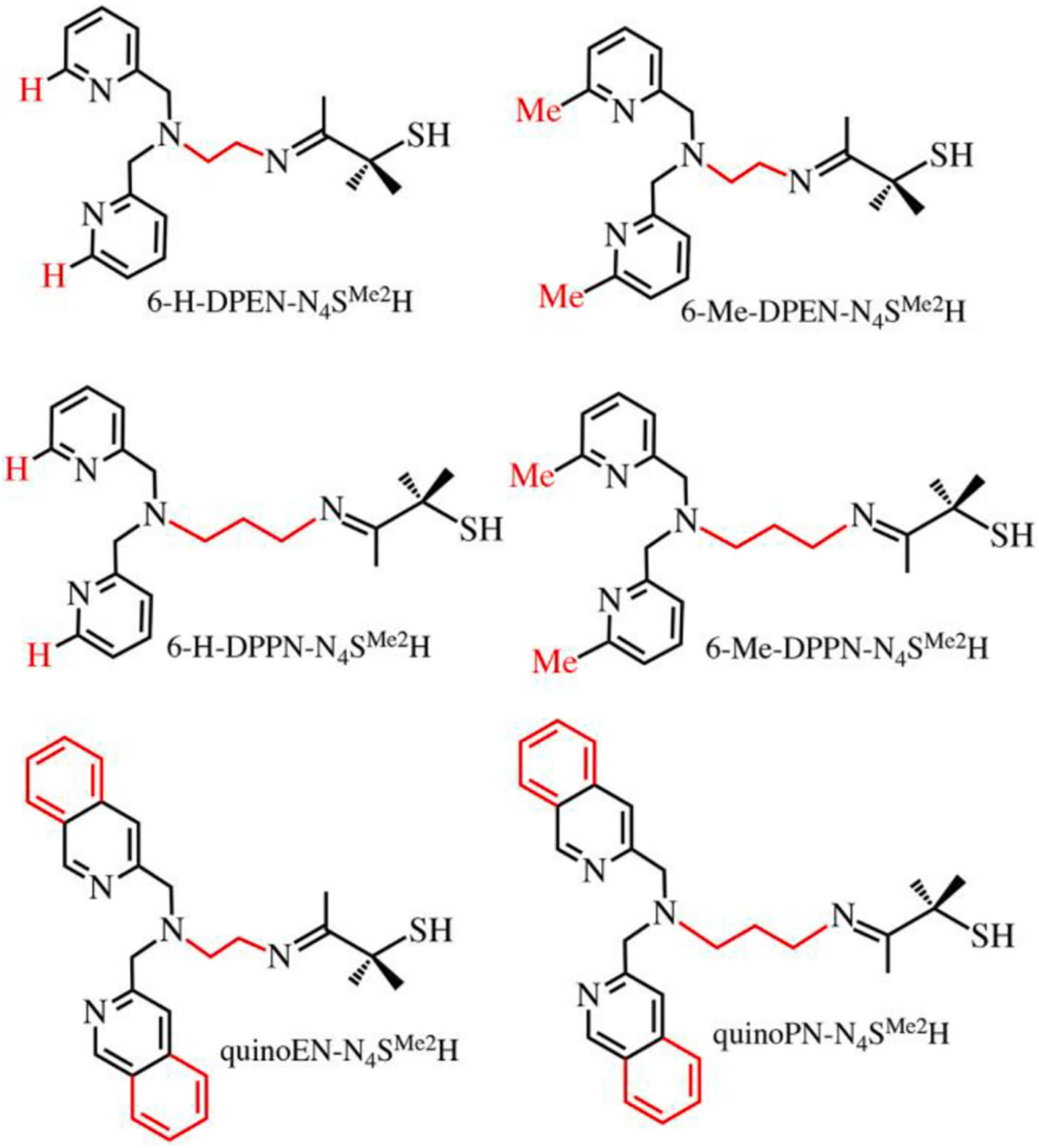

Fig. 4.

Ligands incorporated into the molecules discussed herein. Highlighted in red are the portions of the ligand scaffold that were varied.

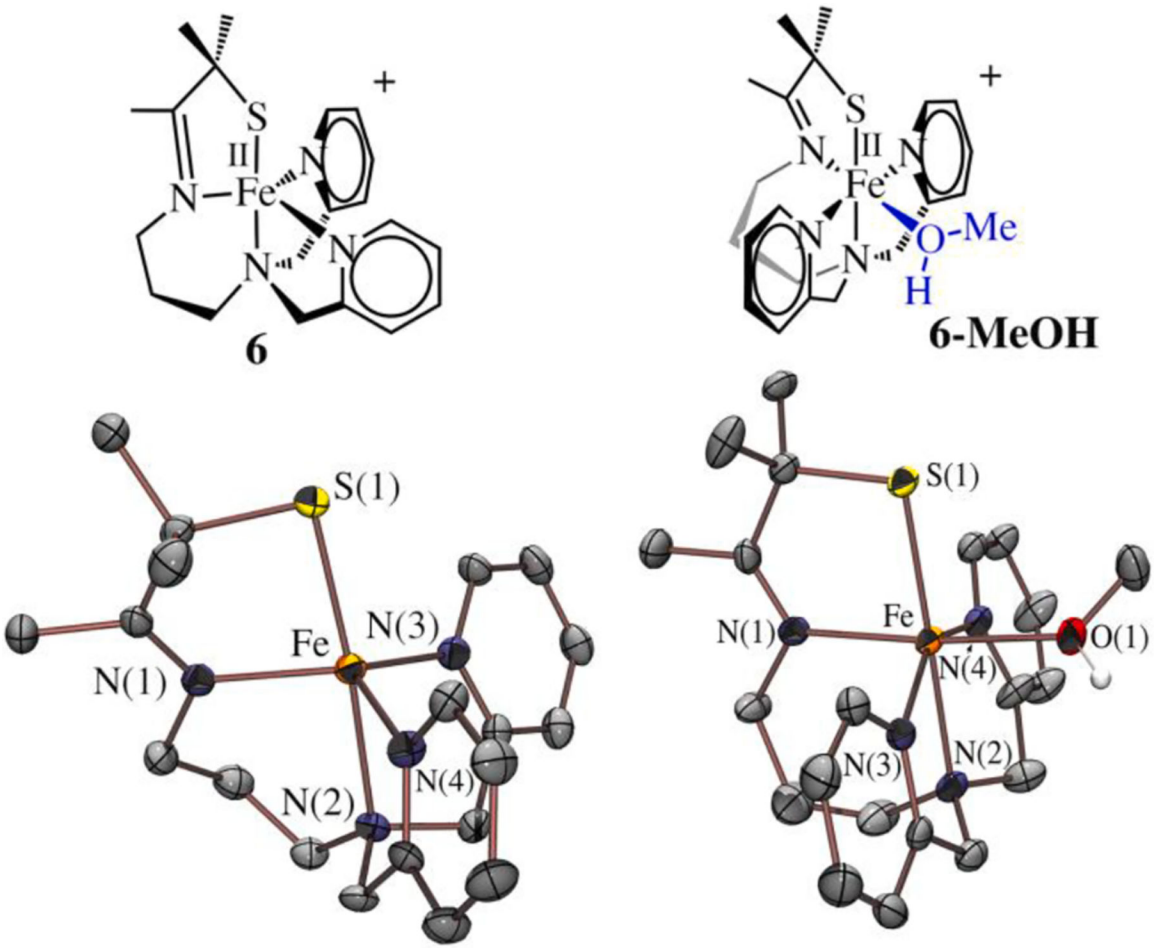

Fig. 5.

ORTEP diagrams of coordinatively unsaturated thiolate-ligated **6** and its MeOH bound derivative **6-MeOH**. Hydrogen atoms, counterions, and cosolvents have been removed, and chemdrawings included for clarity.

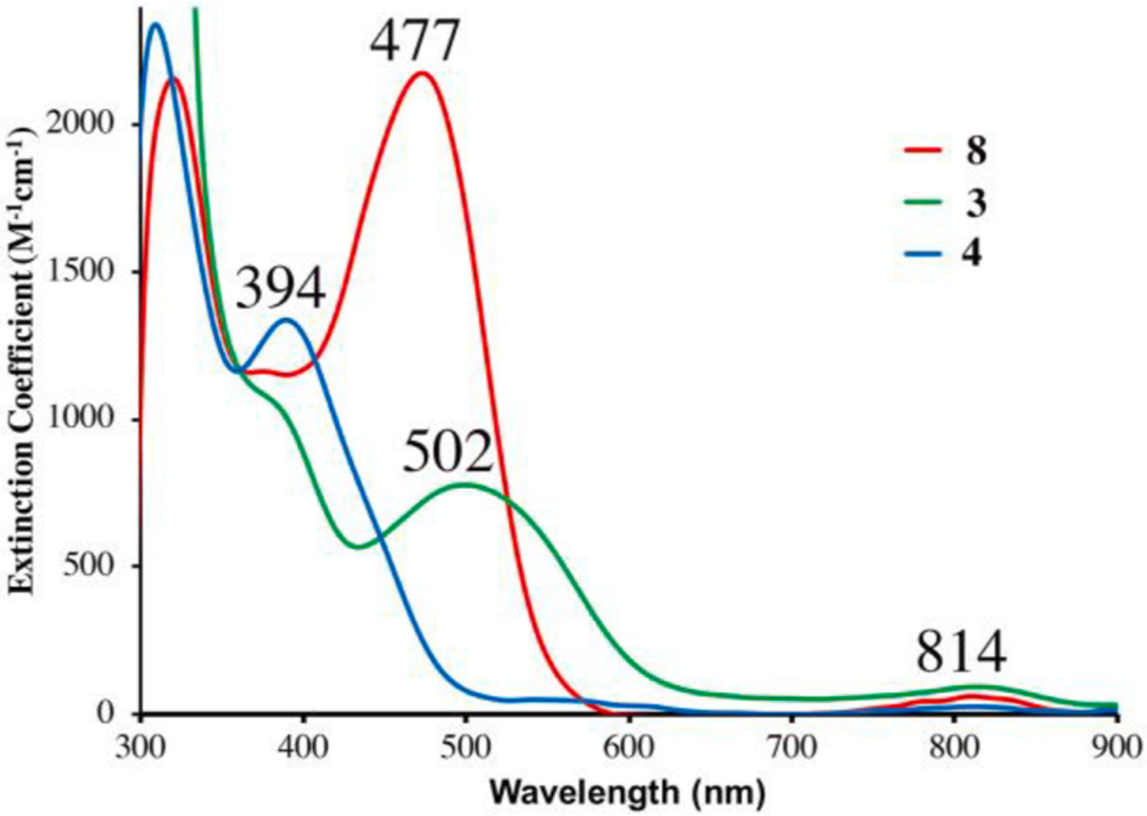

Fig. 6.

Quantitative electronic absorption spectra of **3** (green) and **4** (blue) in THF, and **8** (red) in CH_2Cl_2 at 25 °C.

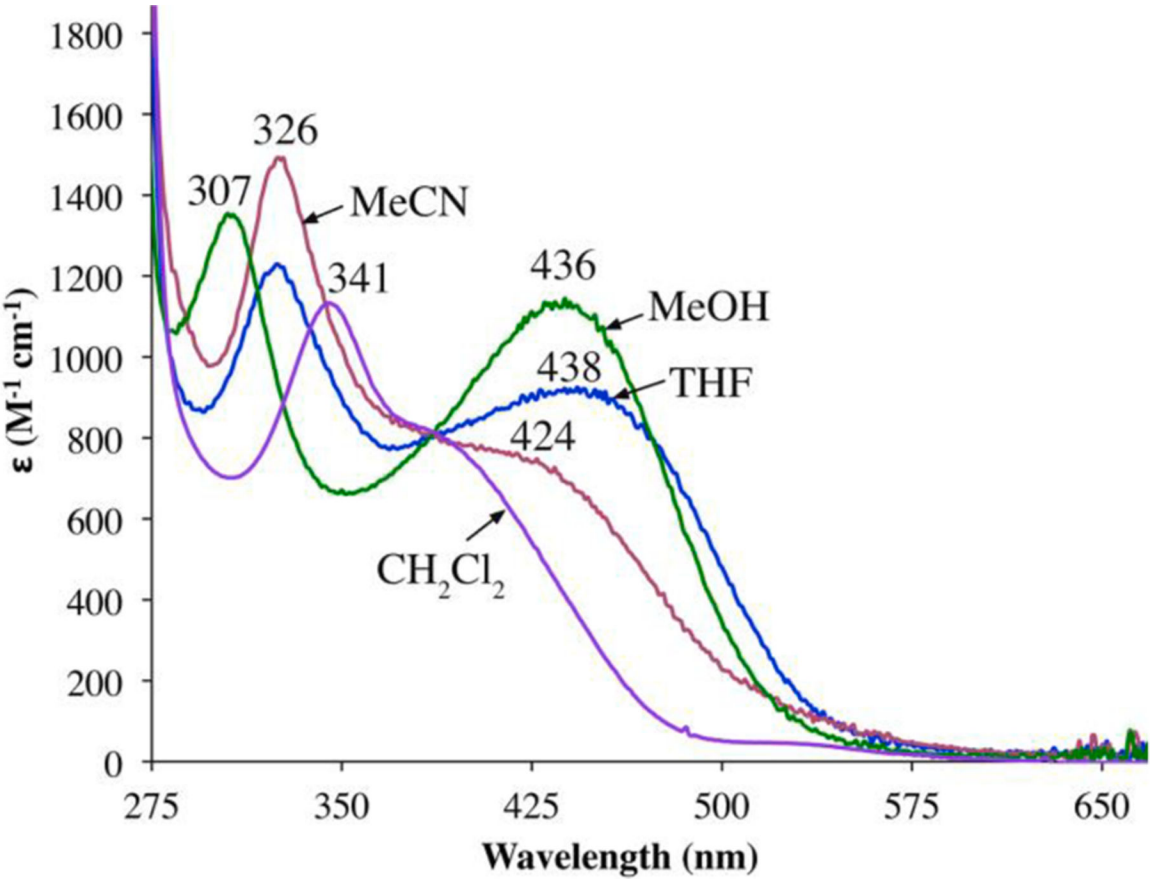

Fig. 7.
Solvent-dependent electronic absorption spectrum of **6** at 298 K.

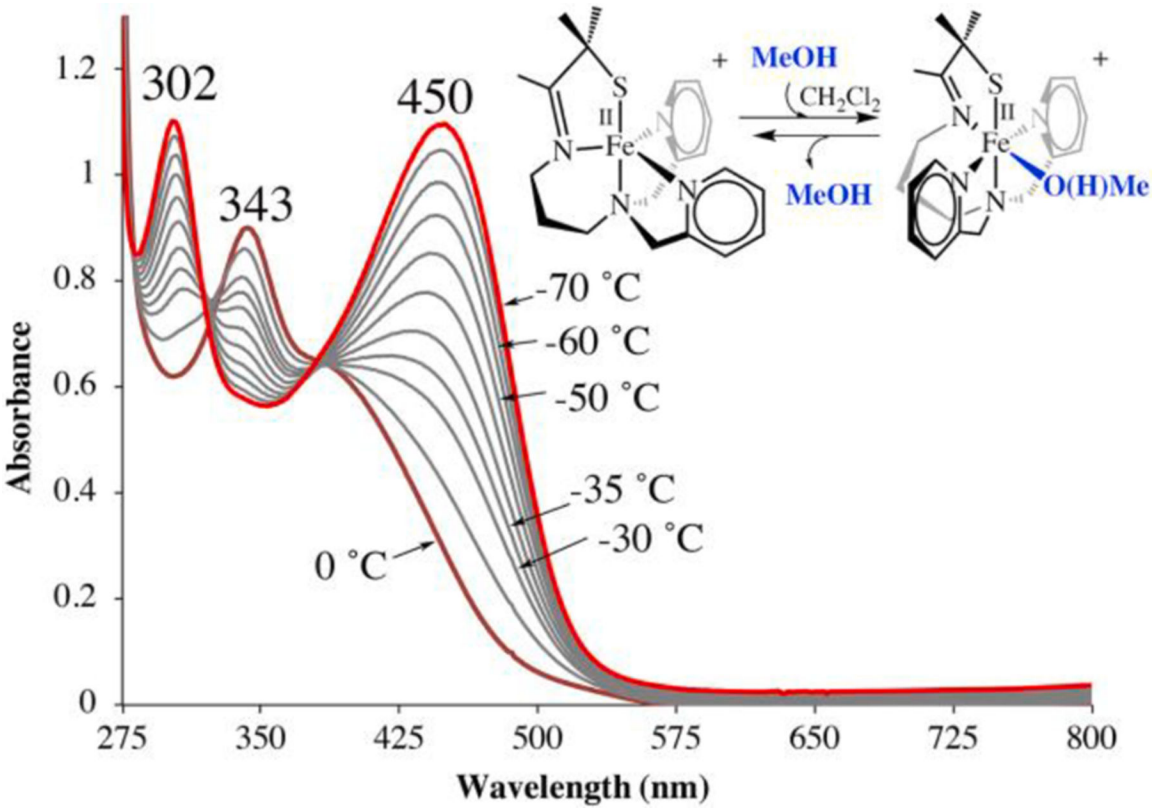

Fig. 8.

Temperature-dependent equilibrium between five-coordinate **6** (0.68 mM) and MeOH-bound **6-MeOH**, formed via the addition of 243 equiv of MeOH to **6** in CH_2Cl_2.

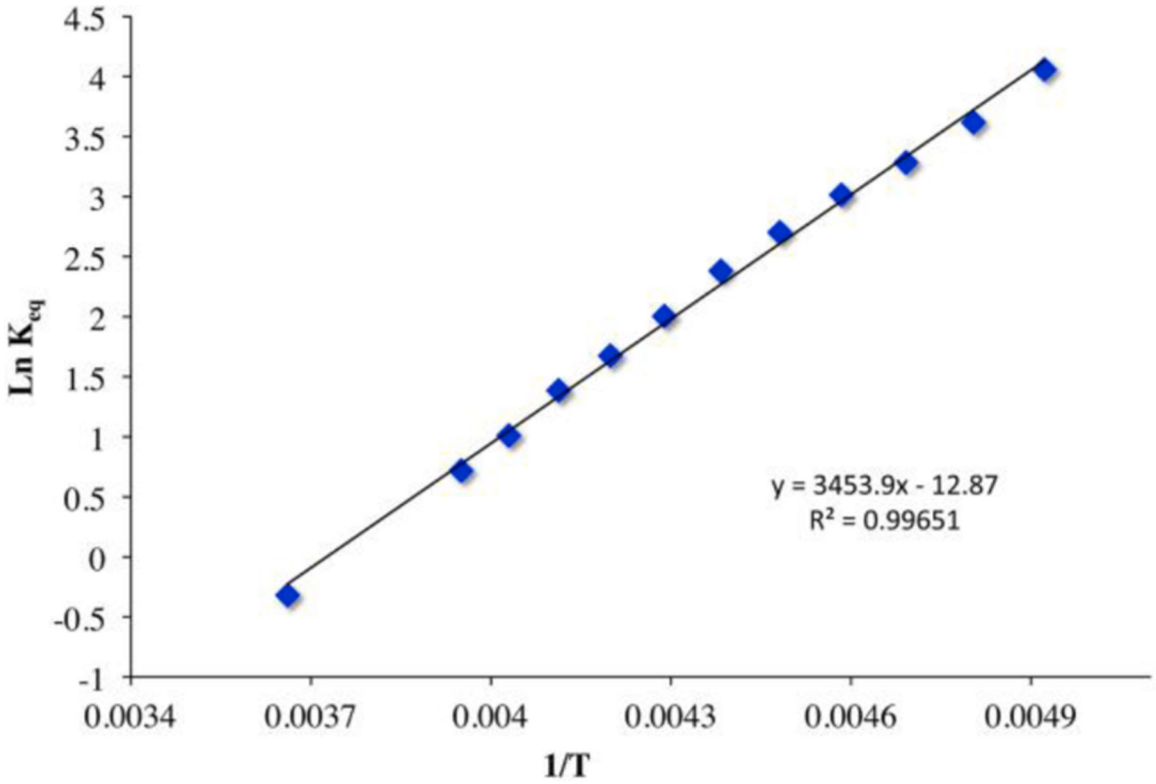

Fig. 9.

Van't Hoff plot for MeOH binding to 5-coordinate **6** in CH_2Cl_2.

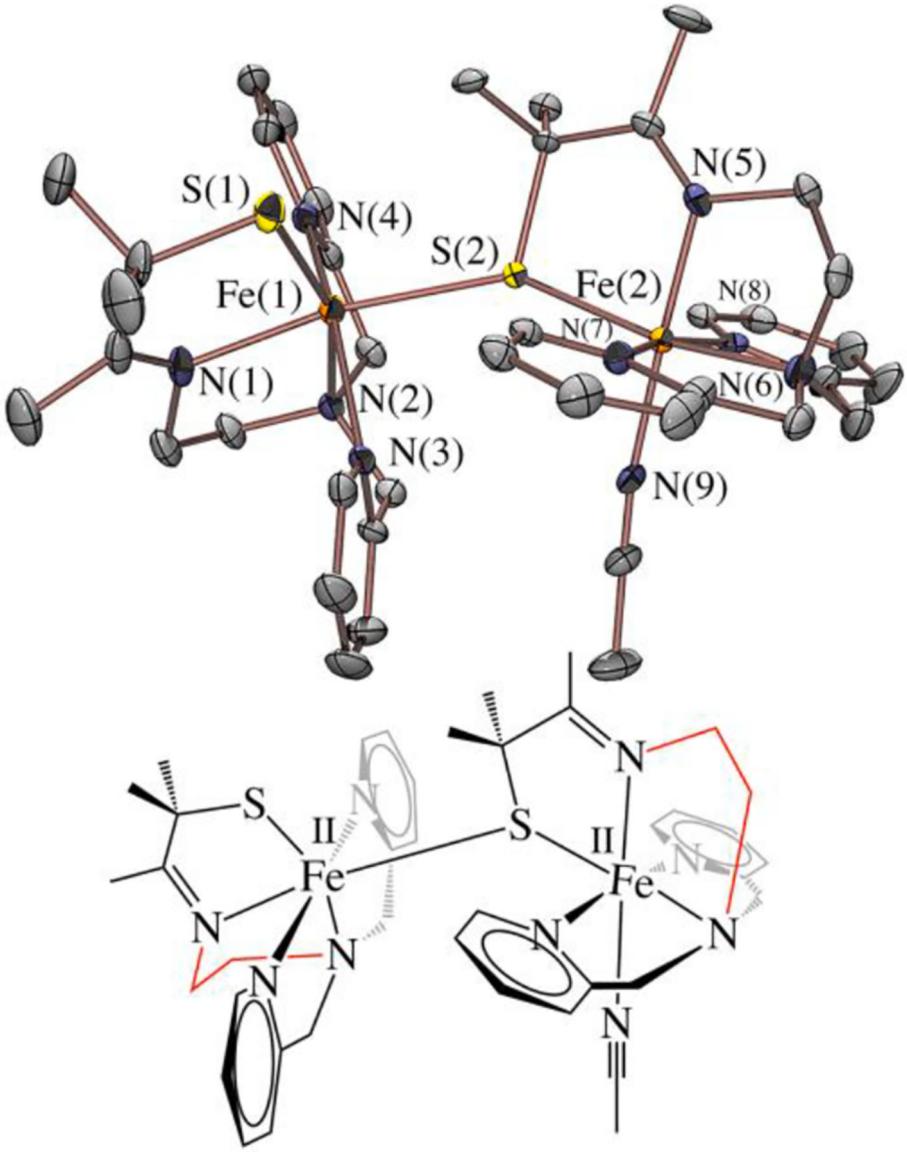

Fig. 10.

ORTEP diagram of thiolate-ligated **8**. Hydrogen atoms, counterions, and cosolvents have been removed, and a chemdrawing was included for clarity.

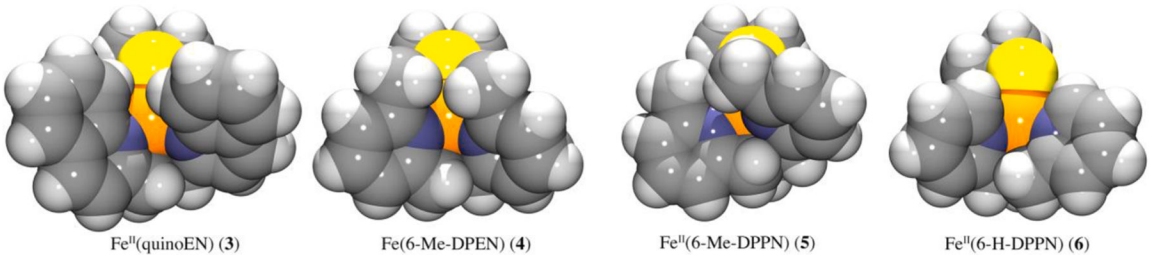

Fig. 11.

Space-filling diagrams comparing metal ion accessibility of sterically encumbered trigonal bipyramidal **3** and **4**, versus sterically encumbered square pyramidal **5**, and unencumbered (6-H substituent) square pyramidal **6**.

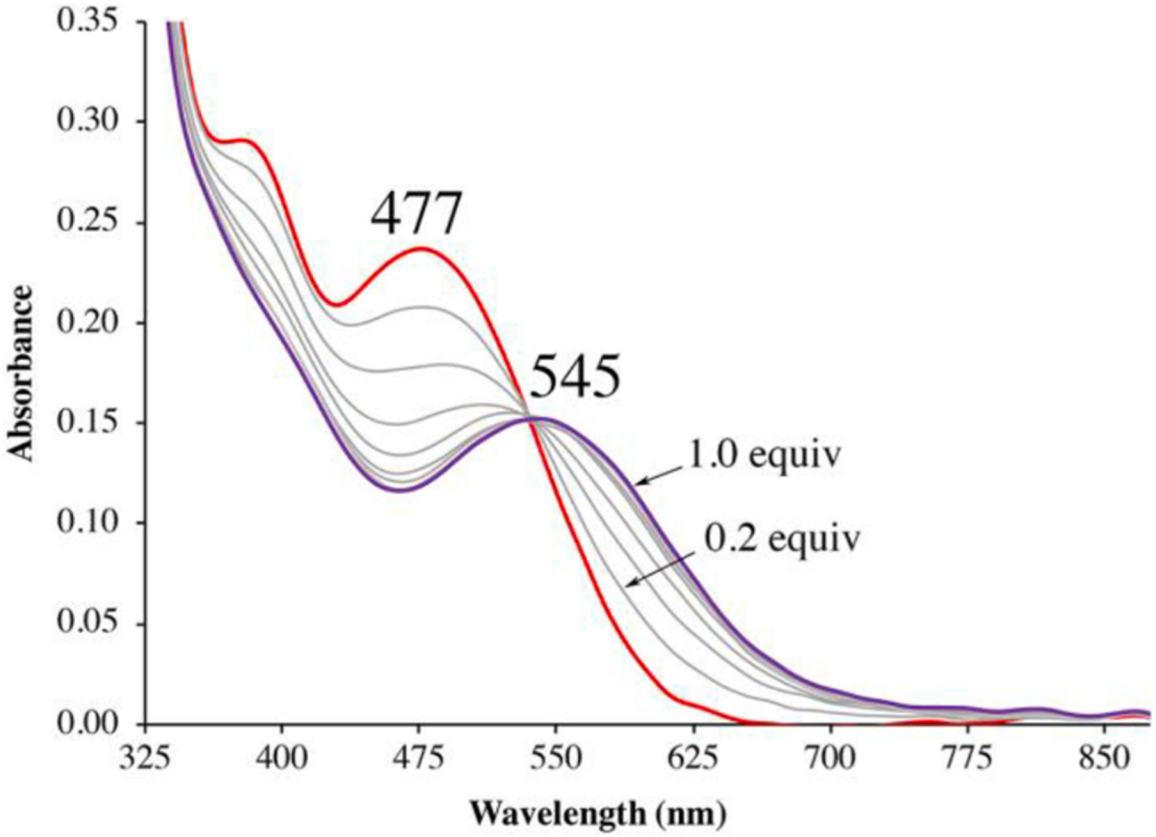

Fig. 12.

Monitoring the addition of Bu_4NOAc (in 0.2 equiv aliquots) to **3** in MeCN at 25 °C by electronic absorption spectroscopy.

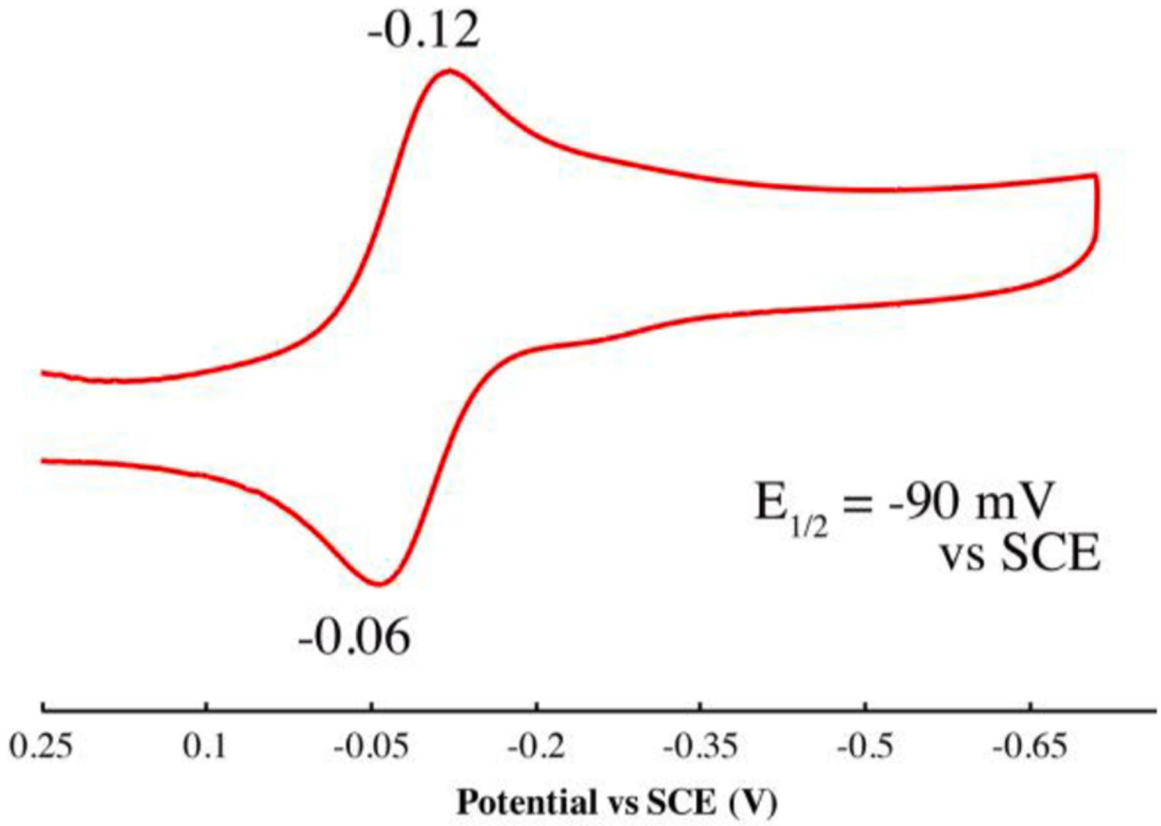

Fig. 13.

Cyclic voltammogram of $[Fe(S^{Me2}N_4(6\text{-H-DPEN}))(MeCN)]^+$ (**8-MeCN**) in MeCN with 0.1 M Bu_4NPF_6 supporting electrolyte, and a scan rate of 100 mVs^{-1}.

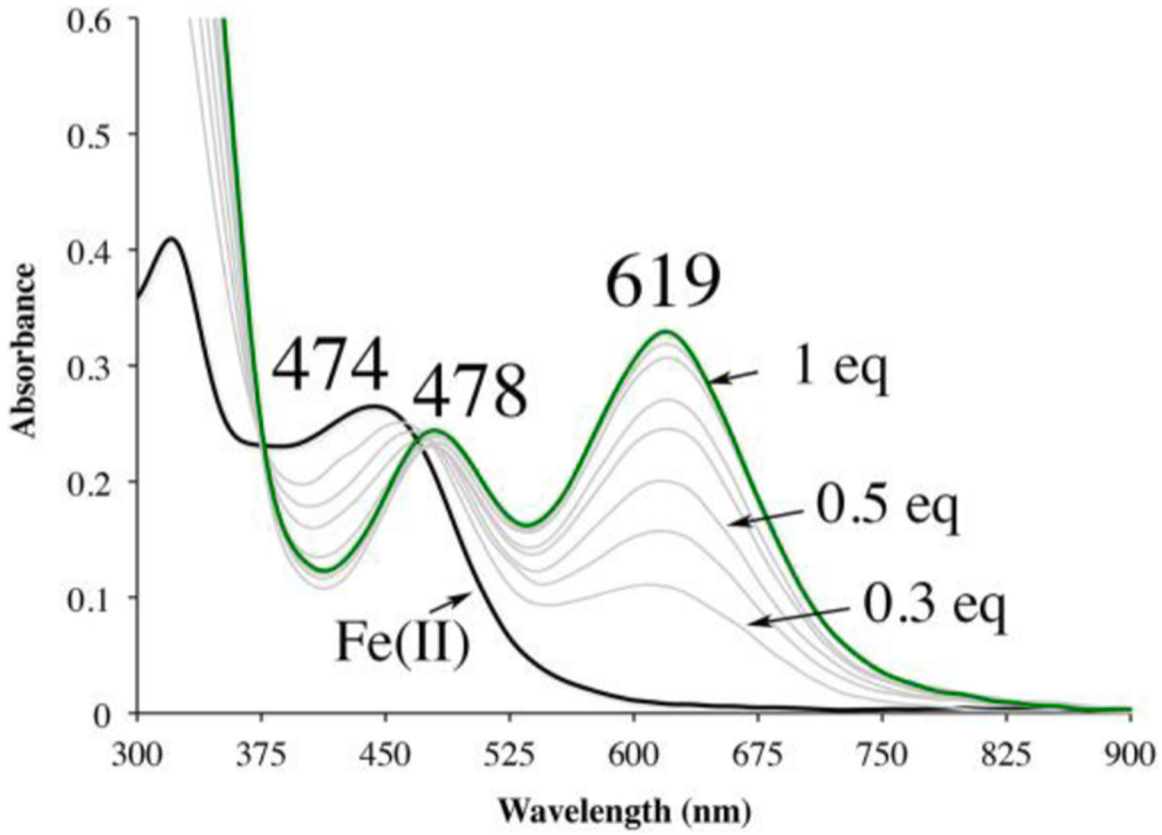

Fig. 14.

Oxidation of 6-H-DPEN **8-MeCN** with (p-tolyliminium)PF_6 in 0.1 eq aliquots in MeCN at 25 °C.

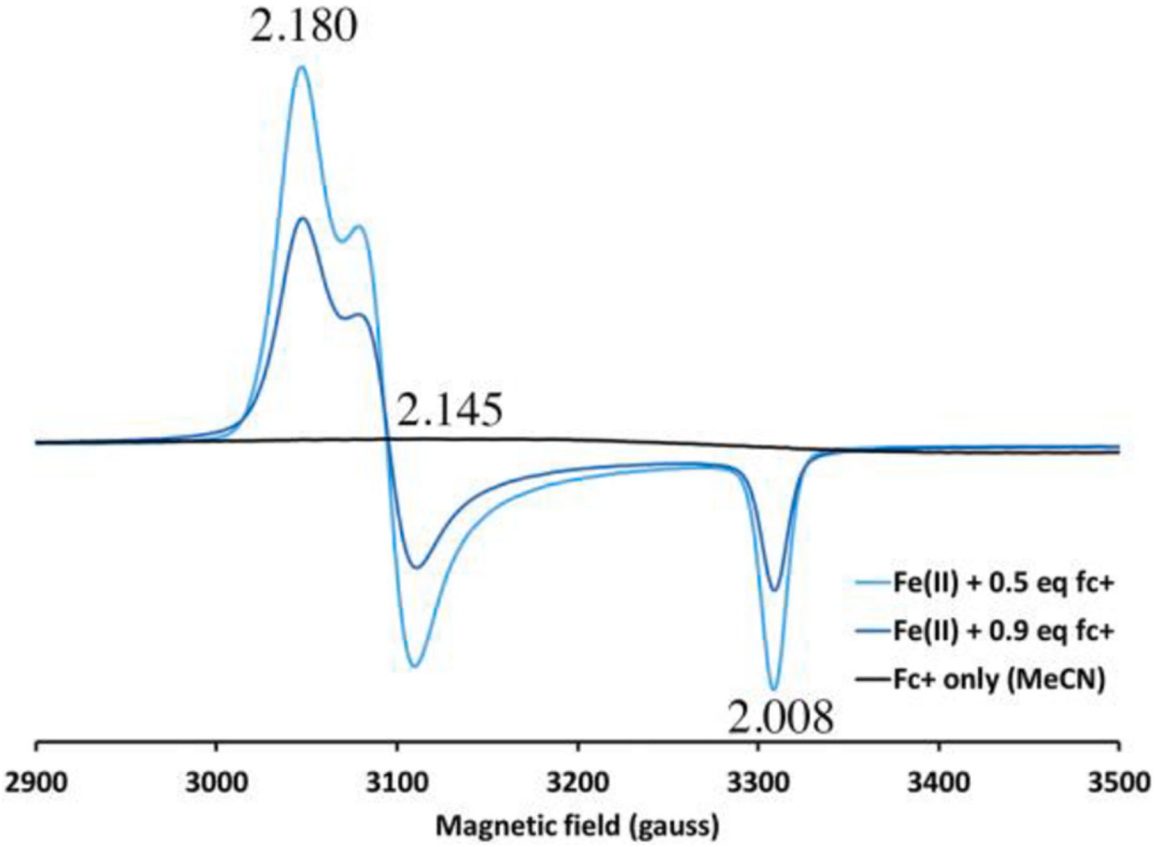

Fig. 15.

⊥-mode, continuous-wave 9.30 GHz EPR spectrum of **8^{ox}-MeCN** in MeCN/toluene glass at 77 K.

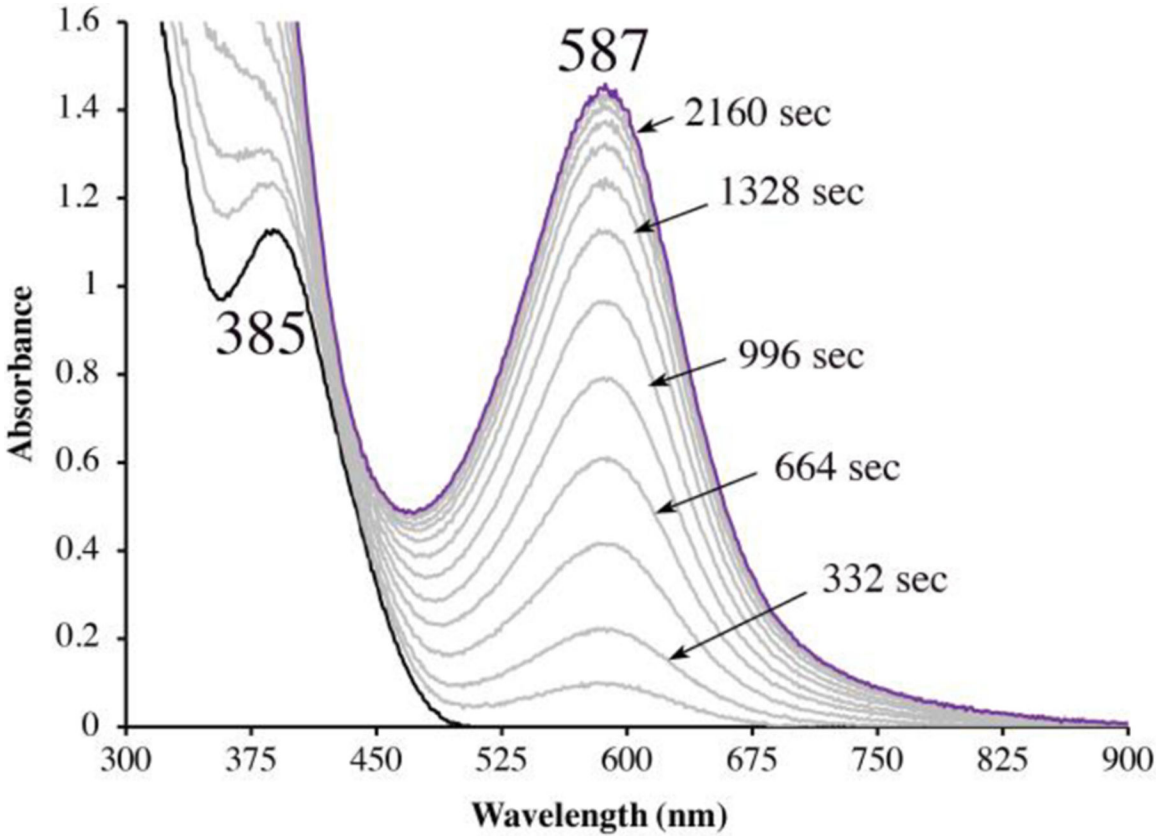

Fig. 16.

Monitoring the addition of O_2 to **4** (black trace) in CH_2Cl_2 at ambient temperature, formation of $\mathbf{4^{\mu\text{-}oxo}}$ (purple trace) was observed over 36 min. Scans recorded at 166 s intervals. [4] = 0.75 mM.

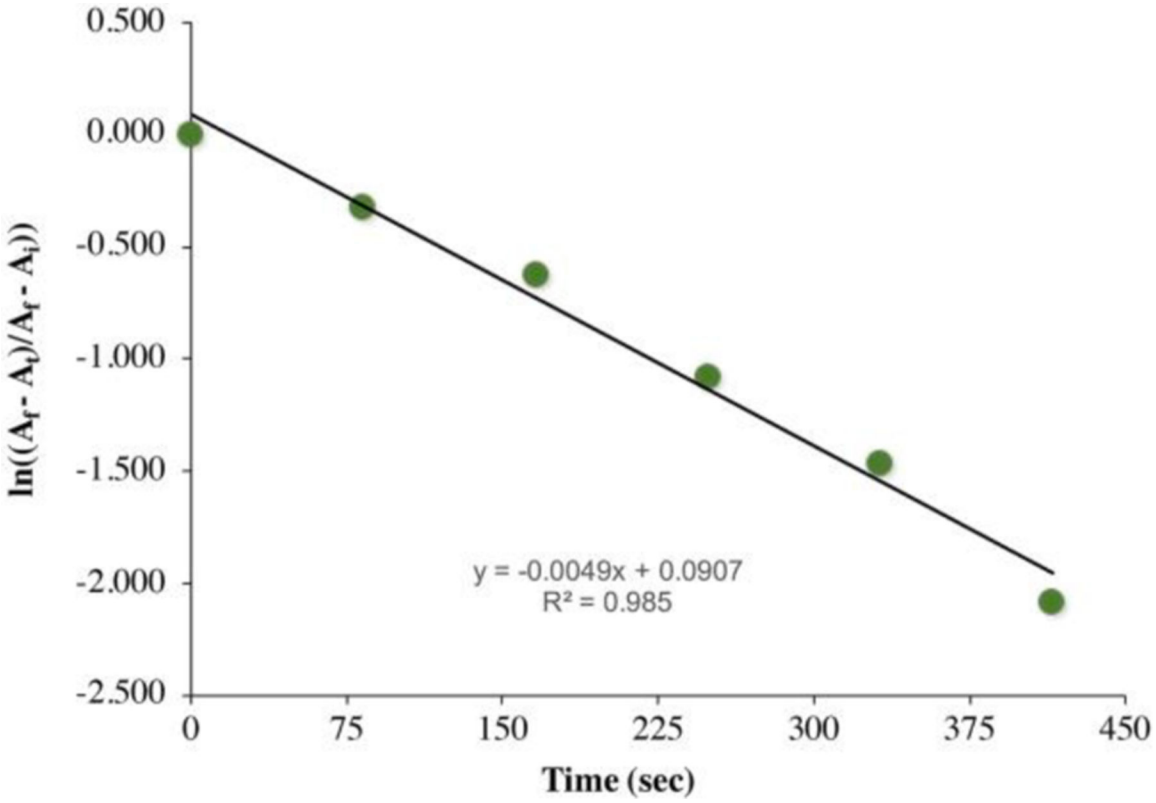

Fig. 17.

First order kinetics plot for the reaction between **3** and O_2 under pseudo 1st order conditions with excess O_2 in CH_2Cl_2 at 25 °C.

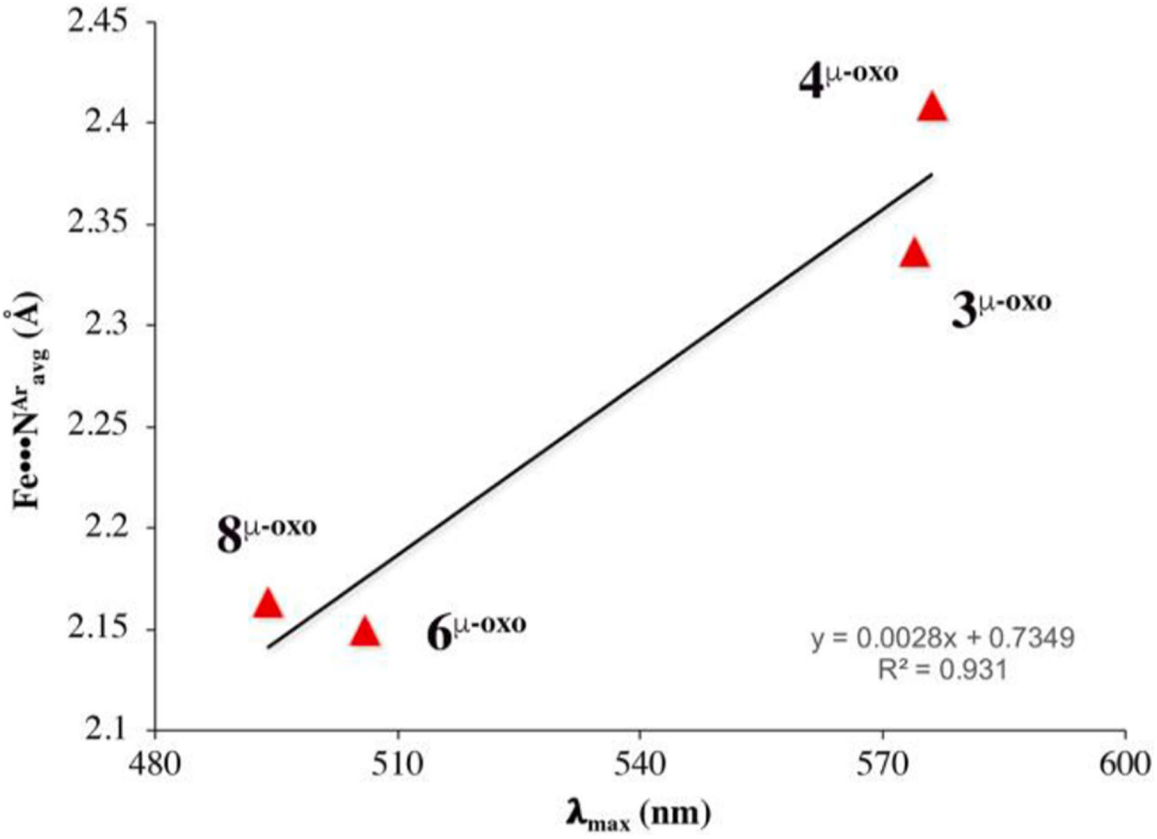

Fig. 18.

ORTEP diagram of oxo bridged **8$^{\mu\text{-oxo}}$** Hydrogen atoms, counterions, and cosolvents have been removed for clarity.

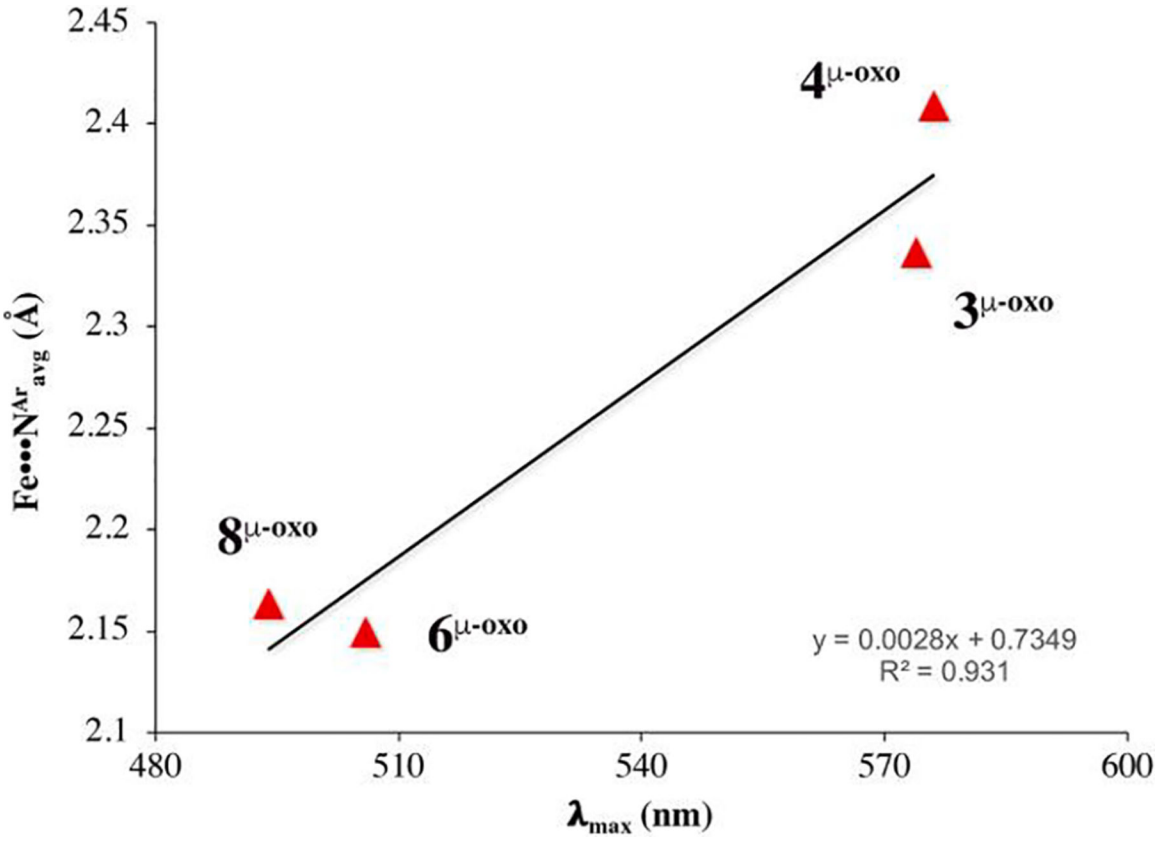

Fig. 19.
Correlation between Fe···N^{Ar} distance and λ_{max} for mono oxo-bridged dimers.

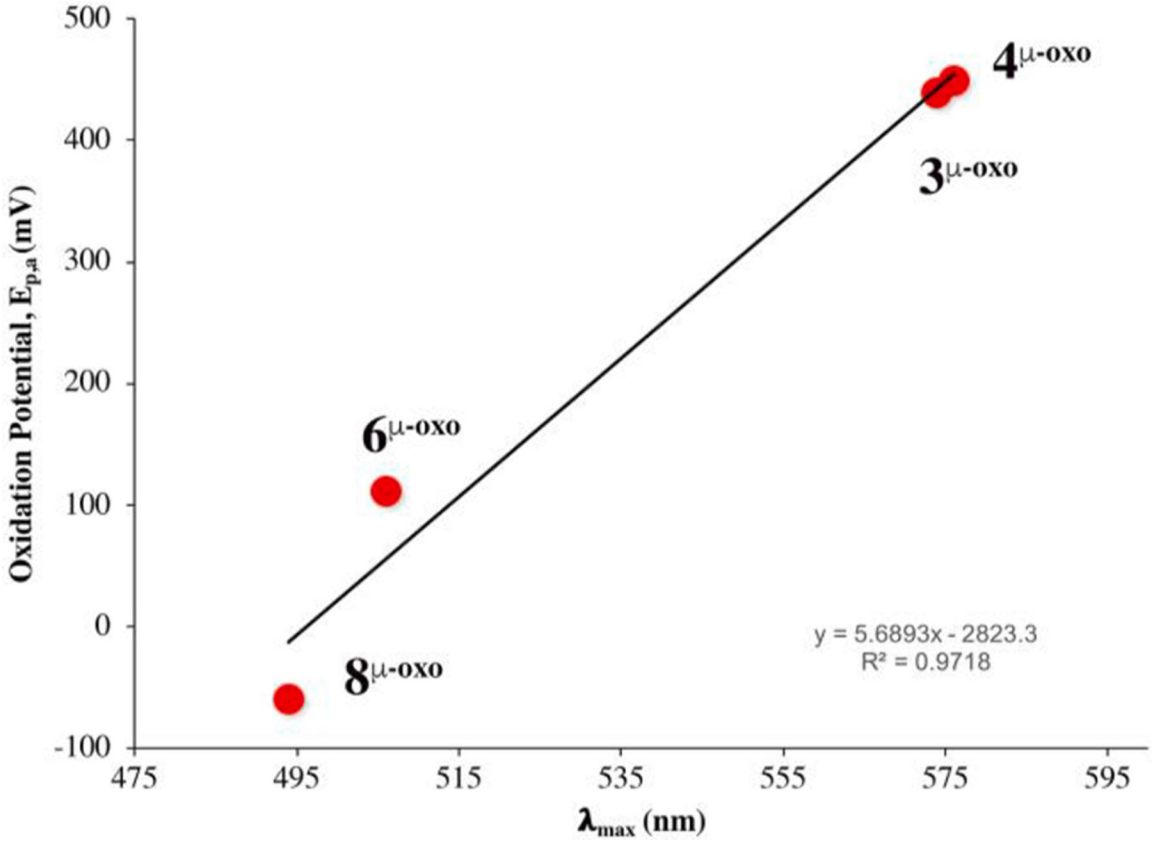

Fig. 20.

Correlation between oxidation potential $E_{p,a}$ distance and λ_{max} for mono oxo-bridged dimers.

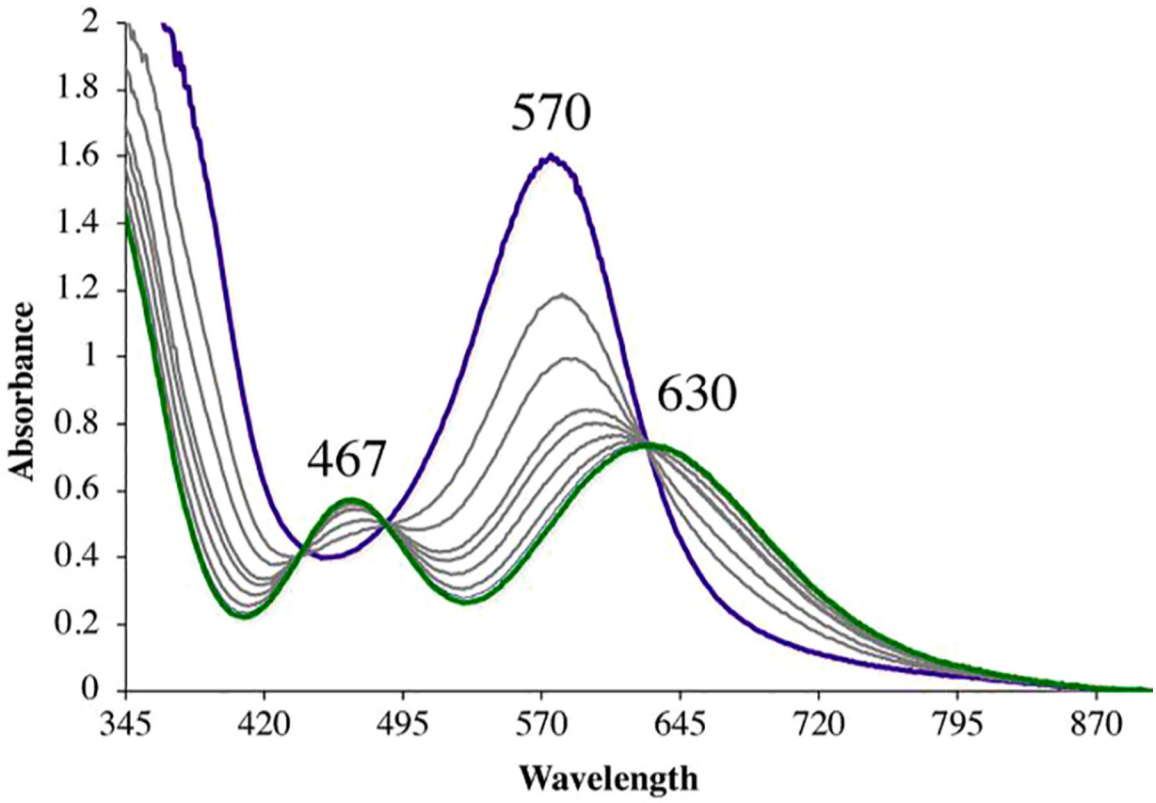

Fig. 21.
Addition of HOAc to **4$^{\mu\text{-oxo}}$** in MeCN at 298 K.

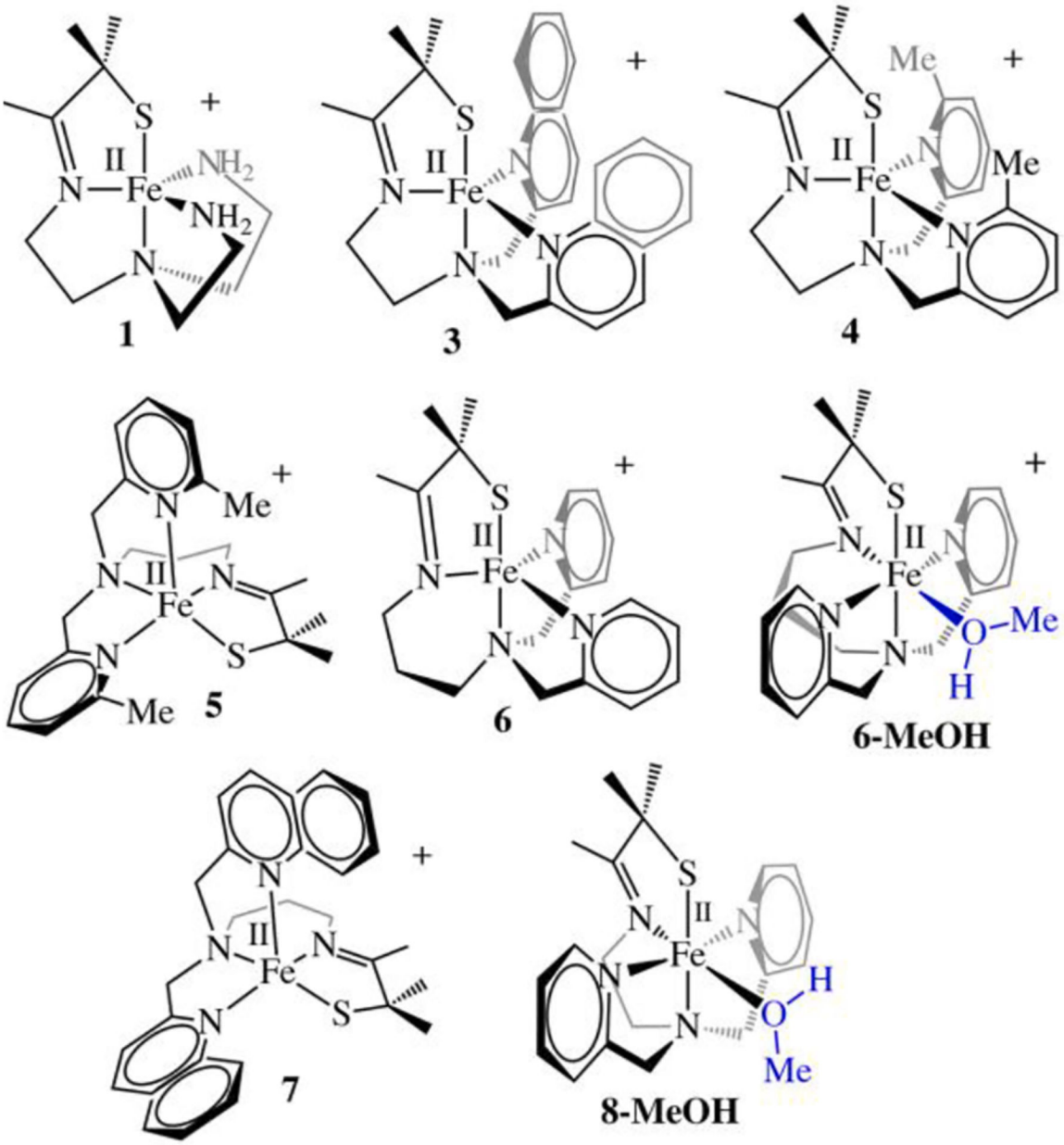

Scheme 1.

ChemDrawings of the Fe(II) complexes discussed herein. The 6th ligand of six-coordinate complexes is highlighted in blue.

Table 1

Selected Bond Distances (Å) and Bond Angles (deg) for Five Coordinate [$Fe^{II}(S^{Me2}N_4$(quinoEN))](PF_6) Et_2O (**3**), [$Fe^{II}(S^{Me2}N_4$(6-Me-DPEN)](PF_6) (**4**), [$Fe^{II}(S^{Me2}N_4$(6-Me-DPPN)](PF_6) (**5**), [$Fe^{II}(S^{Me2}N_4$(6-H-DPPN))] (PF_6) (**6**), and [$Fe^{II}(S^{Me2}N_4$(quinoPN))](BPh_4)·MeCN (**7**).

	3	**4**	**5**	**6**	**7**
Fe-S(1)	2.3357(9)	2.326(1)	2.3005(9)[a]	2.319(1)	2.3057(5)
Fe-N(1)	2.111(2)	2.132(4)	2.155(3)	2.077(3)	2.148(1)
Fe-N(2)	2.226(2)	2.253(4)	2.206(2)	2.299(3)	2.169(1)
Fe-N(3)	2.152(2)	2.165(4)	2.210(3)	2.092(3)	2.226(1)
Fe-N(4)	2.159(2)	2.191(4)	2.133(2)	2.094(3)	2.147 (1)
S(1)-Fe-N(1)	82.91(7)	81.5(1)	83.78(7)	84.00(8)	83.69(3)
S(1)-Fe-N(2)	157.80(6)	158.7(1)	149.70(7)	174.86(8)	148.52(3)
S(1)-Fe-N(3)	106.98(7)	116.1(1)	94.04(7)	106.18(9)	94.28(3)
S(1)-Fe-N(4)	121.74(7)	115.0(1)	129.45(7)	105.73(8)	131.85(3)
N(1)-Fe-N(3)	120.28(9)	123.1(1)	150.42(9)	114.3(1)	154.97(4)
N(1)-Fe-N(4)	119.21(9)	121.0(1)	105.3(1)	126.2(1)	100.55(4)
N(3)-Fe-N(4)	104.91(9)	100.5(1)	98.52	113.1(1)	99.29(4)
τ-value	0.60	0.59	0.01	0.81	0.11

Table 2

Thermodynamic Parameters Associated with Solvent Binding to Five-Coordinate $[Fe^{II}(S^{Me2}N_4(6\text{-H-DPPN})](PF_6)$ (**6**) in CH_2Cl_2.

	MeOH	MeCN	THF
ΔH (kcal/mol)	−6.9(5)	−3.2(1)	−3.27(3)
ΔS (cal/mol·K)	−25(2)	−16(2)	−14.5(1)

Table 3

Comparison of Redox Potentials for Structurally Analogous Thiolate–Ligated Fe (II) Complexes.

	N^{Ar}	Linker	$E_{1/2}$ (mV vs SCE)
$[Fe^{II}(S^{Me2}N_4(tren))]^+$ (**1**)	N/A	Et	−150
$[Fe^{II}(S^{Me2}N_4(6\text{-H-DPEN}))(MeCN)]^+$ (**8-MeCN**)	6-H-DPEN	Et	−90
$[Fe^{II}(S^{Me2}N_4(6\text{-H-DPPN})(MeOH]^+$ (**6-MeOH**)	6-H-DPPN	Pr	+66
$[Fe^{II}(S^{Me2}N_4(2\text{-QuinoEN}))]^+$ (**3**)	QuinoEN	Et	+401
$[Fe^{II}(S^{Me2}N_4(6\text{-Me-DPEN})]^+$ (**4**)	6-Me-DPEN	Et	+408
$[Fe^{II}(S^{Me2}N_4(2\text{-QuinoPN}))]^+$ (**7**)	QuinoPN	Pr	+415
$[Fe^{II}(S^{Me2}N_4(6\text{-Me-DPPN})]^+$ (**5**)	6-Me-DPPN	Pr	+433

Table 4

Selected Bond Distances (Å) and Angles (deg) for oxo bridged binuclear $[Fe^{III}(S^{Me2}N_4(2\text{-quinoEN}))]_2(\mu\text{-O})(BF_4)_2\cdot 2MeCN$ **($3^{\mu\text{-oxo}}$)**, $[Fe^{III}(S^{Me2}N_4(6\text{-Me-DPEN})]_2(\mu\text{-O})(PF_6)_2\cdot$**($4^{\mu\text{-oxo}}$),** $[Fe^{III}(S^{Me2}N_4(6\text{-H-DPEN})]_2(\mu\text{-O})(PF_6)_2\cdot MeCN$ **($8^{\mu\text{-oxo}}$),** $[Fe^{III}(S^{Me2}N_4(6\text{-H-DPPN}))]_2(\mu\text{-O})(PF_6)_2$ **($6^{\mu\text{-oxo}}$)**.

	$3^{\mu\text{-oxo}}$	$4^{\mu\text{-oxo}}$	$8^{\mu\text{-oxo}}$	$6^{\mu\text{-oxo}}$
Fe-S(1)	2.305(1)	2.303(1)	2.306(1)	2.271(1)
Fe-N(1)	2.174(3)	2.163(4)	2.155(3)	2.302(4)
Fe-N(2)	2.175(3)	2.208(4)	2.222(3)	2.240(4)
Fe-N(3)	2.303(3)	2.390(4)	2.160(3)	2.167(4)
Fe-N(4)	2.371(3)	2.429(4)	2.168(4)	2.132(4)
Fe–O	1.778(3)	1.7816(7)	1.787(3)	1.7985(6)
S(1)-Fe-N(1)	80.54(9)	80.3(1)	81.75(9)	79.17(11)
S(1)-Fe-N(2)	158.48(9)	158.8(1)	159.2(1)	168.12(11)
S(1)-Fe-N(3)	104.00(9)	103.63(1)	104.8(1)	99.95(12)
S(1)-Fe-N(4)	104.64(8)	106.9(1)	101.4(1)	106.90(12)
N(1)-Fe-N(3)	83.02(11)	98.1(1)	82.7(1)	91.95(15)
N(1)-Fe-N(4)	95.10(11)	80.5(1)	93.5(1)	87.77(15)
N(3)-Fe-N(4)	150.57(12)	148.7(1)	152.7(1)	152.58(17)
S(1)–Fe–O	104.15(9)	101.84(5)	104.6(1)	97.66(4)
N(1)–Fe–O	173.91(12)	168.7(1)	172.6(1)	171.62(11)
Fe–O–Fe	174.02(14)	180.00	175.9(2)	180.00